Applied Catalysis B: Environment and Energy 395 (2026) 126851

Contents lists available at ScienceDirect

Applied Catalysis B: Environment and Energy

journal homepage: www.elsevier.com/locate/apcatb

The journey of rhodium in Al_2O_3-CeO_2-ZrO_2 supported three-way catalysts

Sarina-Lena Heck [a], Paolo Dolcet [a,b], Gülperi Nails [a], Martin Rösch [c], Ulrich Göbel [c], Nicole Schichtel [c], Andreas Eich [c], Jelena Jelic [d], Felix Studt [d], Maria Casapu [a], Jan-Dierk Grunwaldt [a,d,*]

[a] Institute for Chemical Technology and Polymer Chemistry (ITCP), Karlsruhe Institute of Technology (KIT), Engesserstraße 20, Karlsruhe 76131, Germany
[b] Department of Chemical Sciences, University of Padova, Padova 35131, Italy
[c] Umicore AG & Co. KG, Rodenbacher Chaussee 4, Hanau 63457, Germany
[d] Institute of Catalysis Research and Technology, Karlsruhe Institute of Technology (KIT), Hermann-von-Helmholtz-Platz 1, Eggenstein-Leopoldshafen 76344, Germany

ARTICLE INFO

Keywords:
Rhodium
Migration
Catalyst deactivation
Three-way catalysts
Structural dynamics

ABSTRACT

For increasing the noble metal efficiency and developing more robust emission control catalysts, an accurate understanding of their structural dynamics during operation is essential. This study systematically investigates the manifold interactions of Rh with various catalyst components in alumina/ceria-zirconia based washcoats by advanced *in situ/operando* characterization. Pronounced structural changes, which drastically affect the catalyst performance, were observed during short fuel-cut steps. *Operando* X-ray absorption spectroscopy and electron microscopy investigations revealed the formation of mobile metallic Rh particles under stoichiometric/rich reaction conditions. In contrast, Rh oxidation, volatilization and diffusion into the alumina surface/subsurface occurred above 950 °C during O_2-rich steps. While the first phenomenon contributed to the redistribution of Rh on both supports, the partial relocation of Rh in low-loaded washcoats under lean reaction conditions was exclusively observed to occur from CeO_2-ZrO_2 to γ-Al_2O_3. Overall, the intimate interaction between the washcoat components prevented the loss of the noble metal due to volatilization.

1. Introduction

The loss of activity and selectivity is one of the major concerns during the utilization of heterogeneous catalysts. While the catalyst poisoning is an extrinsic process mostly affected by external factors, thermal deactivation can be prevented or minimized by a careful adjustment of the catalyst composition and synthesis method. Herein, the catalyst structural stability is determined by the evolution of both the carrier material and active species. A strong interaction between the support and active species has been shown to stabilize noble metal-based catalysts against severe sintering [1–3]. Pt and Pd nanoparticles supported on CeO_2 disperse and form strongly anchored single sites in oxygen-rich atmospheres at high temperatures [3–6]. Advanced characterization and density functional theory calculations have shown that Pt is present as substituted Pt^{2+} species on the (110) surface or adsorbed on the (211) surface of CeO_2 while Pd forms substituted Pd^{2+} single sites on the (111) and (110) facets of CeO_2 [6,7]. Highly dispersed species were reported to also form in Rh/CeO_2-based systems under similar conditions [8–10]. Even single crystals of $Ce_{2/3-x}Rh_2O_4$ (x~0.11–0.14) and $CeRh_2O_5$ were synthesized and characterized by Mizoguchi et al. [11]. Nevertheless, above 800 °C the depletion of such Rh single sites and partial segregation was observed by Kibis et al. [12] for Rh/CeO_2 catalysts, in line with the previously reported thermodynamic data for the Ce-Rh-O system at high temperatures [13]. However, if a CeO_2-ZrO_2 solid solution is used as a support, Machida et al. [14] observed the encapsulation of Rh particles upon exposure to dynamic fuel-lean/fuel-rich conditions at 1000 °C, which leads to catalyst deactivation. Besides the interaction with CeO_2, Rh has been reported to diffuse into the subsurface or bulk of Al_2O_3 above 600 °C [15]. This process was associated to the decrease in the reducibility of Rh species and diminishment of the catalyst oxidation activity, while the NO reduction to N_2 seems to be less affected [16,17]. Depending on the temperature range, different noble metal species were claimed to form in a pre-reduced Rh-based catalyst supported on alumina, including surface rhodium oxides at low temperatures and a mixed $Rh(AlO_2)_y$ oxide above 750 °C [18]. Though, the formation of a spinel or the dissolution of Rh species in an O_2-rich atmosphere into the

* Corresponding author at: Institute for Chemical Technology and Polymer Chemistry (ITCP), Karlsruhe Institute of Technology (KIT), Engesserstraße 20, Karlsruhe 76131, Germany.
E-mail address: grunwaldt@kit.edu (J.-D. Grunwaldt).

https://doi.org/10.1016/j.apcatb.2026.126851
Received 15 February 2026; Received in revised form 4 April 2026; Accepted 21 April 2026
Available online 22 April 2026

alumina lattice is challenged by Beck et al. [19], who found Rh species with a similar structure as orthorhombic Rh_2O_3 up to 900 °C while a change in structure was observed with further increase in temperature. Rh_2O_3 nanoparticles were as well reported in previous studies to form during ageing in air for a low surface area α-Al_2O_3 sample [20]. In a more recent study of Li et al. [21] the formation of rhodium aluminate ($RhAlO_x$) above 950 °C was indicated by extensive electron microscopy investigations, and Rh atoms were suggest to occupy sublattice sites of alumina (220) planes. The same study reports the reduction of these species around 800 °C with recovery of the catalyst activity.

Significantly more complex interactions involving the noble metal sites arise when emission control catalysts are formulated with their application-relevant compositions. Considering the broad temperature window of such applications, substantial changes have been implemented in the catalyst composition over the last decades to prevent deactivation. For instance, various dopants like La, Pr, Nd or Zr were shown to improve the thermal stability and postpone the phase transformations for the γ-Al_2O_3 support [22–24]. Similarly, the incorporation of rare earth elements and especially of Zr is employed to increase the thermal stability and oxygen storage capacity of CeO_2 [25–27]. Frequently, alumina- and ceria-based supports are mixed for washcoating of structured emission control catalysts, which allows to exploit both the high surface area and good thermal stability of alumina as well as the high oxygen mobility of CeO_2-ZrO_2 solid solution [28–31]. Due to the limited number of studies on such systems, the intricate interplay between the noble metal and various washcoat components is still an open question. For Pt-based washcoats, the noble metal anchoring as single sites or the formation of clusters on CeO_2-ZrO_2 were observed to occur in Pt/CeO_2-ZrO_2-Al_2O_3 systems [32]. This interaction was also found to inhibit the sintering of Pt in three-way catalysts (TWCs) [31, 33]. Ceria presence affects also the distribution of Pd and the amount of PdO on the surface of a Pd/CeO_2/Al_2O_3 catalyst [34]. This effect was shown to improve the catalytic performance of a Pd/CeO_2-ZrO_2-Al_2O_3 TWCs, and also to help retain the small size of PdO_x species [35]. As previously mentioned, in contrast to Pt and Pd, Rh is known to interact strongly with both alumina and ceria but in different temperature ranges [36]. For a Rh/CeZrLaNd catalyst mixed with a Al_2O_3 binder to form the washcoat, the ageing under rich conditions at 1000 °C was suggested to result in Rh relocation from the CeZrLaNd support towards the boundary with Al_2O_3, which seems to prevent catalyst deactivation by complete encapsulation of Rh particles during lean/rich cycling [14]. The movement of Rh between CeO_2-ZrO_2 and Al_2O_3 and vice versa was also reported after hydrothermal ageing of mechanically mixed washcoats at 1000 °C for 10 h under humid air flow [37]. Under these conditions, the formation of $RhAlO_x$ species has been previously correlated to the TWC deactivation [17,21]. All in all, a broad spectrum of ageing effects has been identified, mostly derived from post-mortem characterization of differently tested or aged emission control catalysts. These include noble metal sintering, migration, encapsulation, support surface/subsurface incorporation and solid-state reactions. Despite this complex outcome seems to be dictated by the multifaceted interactions, a comprehensive evaluation of catalyst structural changes directly at high temperatures under harsh and dynamic operating conditions is still lacking. Herein, the use of *operando* characterization methods that enable the identification of such structural variations for realistic catalyst composition containing very low noble metal loadings is essential.

In this context, our study aims to elucidate the fate of the noble metal in Rh/γ-Al_2O_3+CeO_2-ZrO_2 and Rh/CeO_2-ZrO_2+γ-Al_2O_3 three-way catalyst washcoats by tracking its structural evolution under realistic operating conditions and comparing these changes with those induced by long-term ageing. For this purpose, thorough *in situ/operando* characterization was combined with systematic catalyst ageing and activity tests. In addition to hydrothermal ageing of mixed/unmixed/spatially separated Rh/γ-Al_2O_3 and Rh/CeO_2-ZrO_2 catalysts, the evolution of Rh species under fuel-cut ageing conditions was evaluated by *operando* X-ray absorption spectroscopy (XAS). Such short interruptions of fuel injection (fuel-cut), which cause combined thermal and chemical stress on the catalyst, are typically applied to reduce the fuel consumption and corresponding CO_2 emissions in gasoline engines. Additional information on the entire catalytic system was obtained via electron microscopy, X-ray diffraction (XRD), elemental analysis and temperature programmed reduction/reoxidation studies. Finally, the holistic understanding of the noble metal-support interplay was refined by density functional theory (DFT) calculations.

2. Experimental section

2.1. Catalyst preparation

Catalyst powders: Commercial γ-alumina with a specific surface area (SSA) of 140 m^2/g and pore volume of 0.5 ml/g and commercial lanthanum-doped ceria-zirconia mixed oxide with 10 wt% La_2O_3, 24 wt % CeO_2 and 66 wt% ZrO_2 and a SSA of 80 m^2/g and pore volume of 0.7 ml/g were used as carrier materials. In a first step, the supports were calcined at 700 °C for 5 h prior to the addition of the noble metal precursor by incipient wetness impregnation. An aqueous rhodium (III) nitrate solution (10 wt% Rh in HNO_3, Acros Organics) was added dropwise to the γ-Al_2O_3 and $CeZrLaO_2$ supports to obtain a final noble metal loading of 1 wt%. The resulting samples were dried at 70 °C for 1 h and calcined at 500 °C for 5 h in static air. In the following, the obtained catalysts are referred to as Rh/Al_2O_3 and Rh/CeZrLa.

Washcoats: the calcined γ-Al_2O_3 and CeZrLa supports were manually mixed (MM) with the 1 wt% Rh/CeZrLa or with 1 wt% Rh/γ-Al_2O_3 catalysts, respectively, in a wt% ratio of 1: 1. The obtained samples are denoted MM:Rh/Al_2O_3-CeZrLa and MM:Rh/CeZrLa-Al_2O_3 in the following. A second set of washcoats was prepared by ball milling the respective powder mixtures 5 times for 1 min with 300 rpm in a ZrO_2 crucible with ZrO_2 balls. These samples are referred to as BM:Rh/Al_2O_3-CeZrLa and BM:Rh/CeZrLa-Al_2O_3, respectively.

Hydrothermal ageing (HA): The as prepared catalyst powders and washcoats were hydrothermally treated in 10% O_2, 5% H_2O / N_2 at 1050 °C for 12 h with a total gas flow of 2 L/min. The corresponding samples are denoted HA-"sample acronym". To evaluate the noble metal migration, in a second ageing procedure the Rh/CeZrLa and Rh/Al_2O_3 catalysts were spatially separated from the pure Al_2O_3 or CeZrLa supports, respectively. The γ-Al_2O_3 and CeZrLa supports were placed downstream the Rh/CeZrLa and Rh/Al_2O_3 catalysts, separated by quartz wool. In this case, hydrothermal ageing was applied at 950 °C and 1050 °C for 12 h each and additionally at 1050 °C for 24 h in a total gas flow of 1 L/min containing 10% O_2, 5% H_2O/ N_2. These samples are denoted "sample acronym" – 950 °C (1050 °C)/12 h (24 h).

2.2. Catalytic activity tests

The catalytic activity was evaluated using 200 mg of the granulated (125–250 μm) fresh or aged washcoat powder mixed with 800 mg of granulated (125–250 μm) quartz in a plug flow reactor with an inner diameter of 0.8 cm and an outer diameter of 1.0 cm. The temperature was regulated using a thermocouple positioned approximately 0.2 cm upstream of the catalyst bed, whereas a second thermocouple was placed at the same distance downstream of the catalyst bed to record the temperature variations induced by the catalytic reaction. Maintaining the same amount of noble metal in the reactor, additional tests were conducted for the pure catalysts using 100 mg of granulated samples mixed with 900 mg of granulated quartz. Light-off/light-out tests were performed for the fresh samples by heating the catalyst bed in a stoichiometric gas feed ($\lambda = 0.998$) containing 3000 ppm CO, 1000 ppm NO, 1000 ppm C_3H_6, 5400 ppm O_2, 10 % H_2O and N_2. Three consecutive light-off/light-out cycles were conducted up to 500 °C, 800 °C and 950 °C with 10 °C/min ramp rate at a noble metal weight hourly space velocity of 60,000 $L \cdot g_{Rh}^{-1} \cdot h^{-1}$. Analogously, the catalytic activity of the hydrothermally aged catalysts was evaluated during three consecutive

light-off/light-out cycles up to a maximum temperature of 800 °C. The gas concentration in the product flow was monitored online by a Fourier transformed infrared spectrometer (MultiGas™ 2030 FTIR Gas Analyser, MKS Instruments) and a mass spectrometer (Pfeiffer Vacuum OmniStar GSD-320).

2.3. Catalyst characterization

Inductively coupled plasma optical emission spectroscopy (ICP-OES): The elemental composition of the prepared samples was determined by ICP-OES on an iCAP 7600 DUO Thermofisher Scientific system at the Institute for Applied Materials Physics (IAM-AWP) of KIT. For this purpose, the samples were digested in the pressure digestion system DAB-2. The measurements were repeated three times for accuracy.

Electron microscopy: The noble metal particle size distribution was studied by high-angle annular dark-field (HAADF) scanning transmission electron microscopy (STEM) at the Laboratory for Electron Microscopy (LEM) of KIT. A FEI OSIRIS ChemiSTEM Microscope with 200 kV acceleration tension was used, which was equipped with a Bruker Quantax system (XFlash detector) for energy-dispersive X-ray spectroscopy (EDXS) measurements. For the analysis of the catalysts, the sample suspension in deionized water was deposited onto carbon coated Cu grids.

X-ray diffraction (XRD) – Measurements were done for all samples using a Bruker Advance D8 diffractometer with Cu Kα ($\lambda = 0.154$ nm) radiation and a VÅNTEC-1 detector with Cu K_β filter. The scanning range was from 10 ° to 120 ° with a step size of 0.016 ° and a dwell time of 3 s.

Temperature programmed reduction/reoxidation (H_2-TPR/TPO) tests were conducted on an AutoChem II Chemisorption Analyzer (Micromeritics) using a thermal conductivity detector (TCD) to monitor the variations in the gas composition (i.e. H_2 consumption). H_2-TPR experiments were performed in 10% H_2/Ar between room temperature and 950 °C while applying a temperature ramp of 10°C/min and a gas flow of 50 ml/min. After sample reoxidation in 10% O_2/Ar for 10 min at 500 °C, another H_2-TPR test was conducted with the same parameters. In the case of HA-Rh/γ-Al_2O_3, a mild thermal treatment in 10% O_2/Ar at 500 °C was additionally conducted prior to the H_2-TPR to remove the adsorbed species, i.e. H_2O.

X-ray absorption spectroscopy (XAS): *Ex situ* XAS data were acquired at the Rh K-edge (23,220 eV) at the BM23 Beamline of the European Synchrotron Radiation Facility (ESRF). *In situ/operando* XAS measurements were conducted at the ROCK and SAMBA beamlines of the SOLEIL synchrotron. For these measurements 5 mg catalyst/washcoat powders (125–250 μm sieved fraction) were placed in a plug-flow quartz capillary reactor with an inner diameter of 1.46 mm and an outer diameter of 1.5 mm. The temperature of the reactor was regulated using a thermocouple positioned approximately 0.1 cm upstream of the catalyst bed. Analogous to the laboratory tests, several light-off/light-out cycles were conducted with a ramp rate of 10 K/min in a close to stoichiometric gas feed ($\lambda = 0.998$) containing 3000 ppm CO, 1000 ppm NO, 1000 ppm C_3H_6, 5400 ppm O_2, approx. 2% H_2O in He (details cf. scheme S1). The highest temperatures applied were 500 °C and 1000 °C for the first two consecutive light-off/light-out cycles, respectively. For simulating the fuel-cut conditions, the gas feed was switched six times at 1000 °C during the second activity cycle between the stoichiometric reaction mixture and oxidizing conditions (10% O_2, approx. 2% H_2O in He) with a holding time of 15 min for each step. After the final switch the catalyst was cooled down to room temperature in the reaction mixture. In a third cycle the catalyst was heated to 1000 °C in stoichiometric atmosphere and the fuel-cut procedure was applied once again. In this case, the catalyst bed was cooled down to room temperature under oxidizing conditions. Finally, a fourth light-off/light-out cycle was conducted that included heating to 800 °C and cooling to room temperature under stoichiometric reaction conditions. The gas concentrations at the reactor outlet were monitored online by a Fourier transformed infrared spectrometer (MultiGas™ 2030 FTIR Gas Analyser, MKS Instruments) and a mass spectrometer (Pfeiffer Vacuum OmniStar GSD-320). Before and after each light-off/light-out cycle, EXAFS measurements were conducted at room temperature to analyse the state of the catalyst after the different reaction conditions.

Data processing was carried out with the Athena software of the Demeter software package (version 0.9.26) and the Fastosh software of the SAMBA beamline (version v1.0.6) [38,39]. For the wavelet transform EXAFS analysis (WT-EXAFS), the k^2-weighted EXAFS data in the 1–14 $Å^{-1}$ range were used. Wavelet transform analysis was conducted with the MorletE software [40,41] with $\eta = 5$, $\sigma = 2$, $k_{min} = 2.5$, $k_{max} = 14$, $r_{min} = 1$ and $r_{max} = 6$. Linear combination analysis (LCA) was performed for the normalized *in situ/operando* XANES data in the −20 eV to 30 eV energy range around E_0 using Rh bulk oxides and foil as references. R-factors < 0.005 and reduced $\chi^2 < 0.05$ were obtained for all data sets, with the CeZrLa supported samples showing the largest values.

Density functional theory (DFT) calculations were performed using the Vienna ab initio simulation package (VASP) [42,43] in connection with the Atomic Simulation Environment (ASE) [44]. The projector augmented wave (PAW) [45,46] method and the Bayesian Error Estimation Functional with van der Waals correlations (BEEF-vdW) [47] exchange-correlation functional were employed. The plane wave cutoff energy was 400 eV in all calculations. Bulk Rh, Rh_2O_3 and RhO_2 were optimized with a 8 × 8×8 Monkhorst-Pack k-point sampling [48]. A correlation was determined between the Bader charge and Rh oxidation state in the bulk references, which was used to estimate the oxidation state of individual adsorbed or substituted RhO_x species on different support oxides (Fig. S14). Surfaces (CeO_2(111) and the crystalline Digne model [49] of dehydrated γ-Al_2O_3(110)) have been optimized using 4 layers thick 2 × 2 large unit cells, with the two top layers (with and without adsorbed single RhO_x species) being allowed to relax, while the bottom two layers have been kept fixed at the bulk positions. Monoclinic θ-Al_2O_3 (100) surface was modeled using 6 layers thick 3 × 2 large unit cell, with each layer being allowed to relax. Monoclinic ZrO_2(101) surface was modeled using 3 layers thick 2 × 2 large unit cells, with the two top layers being allowed to relax, while the bottom layers have been kept fixed at the bulk position. Geometries were optimized until the forces were less than 0.01 eV/Å. For the surface models we have used 4 × 4×1 Monkhorst-Pack k-point sampling.

3. Results and discussion

3.1. Structure and catalytic behaviour of the fresh catalysts and washcoats

To identify structural changes induced by catalyst aging, the initial states of the noble metal and supports were evaluated first. The XRD patterns collected for the as prepared catalysts (Fig. 1a) displayed only the characteristic patterns of the used support materials CeO_2-ZrO_2-La_2O_3 and γ-Al_2O_3, revealing the presence of highly dispersed noble metal species in both samples. Similar XRD patterns were obtained for the ball milled and manually mixed Rh/Al_2O_3-CeZrLa and Rh/CeZrLa-Al_2O_3 washcoats, indicating that the preparation method did not alter the initial structure of the support materials and catalysts (Fig. 1a and S1). Indeed, the corresponding XAS measurements at the Rh K-edge (Fig. 1b) for the catalyst powders and washcoats identified Rh^{3+} and Rh^{4+} as the main species in the alumina and ceria-zirconia supported samples, respectively, after the preparation. The presence of different oxidation states for Rh on the alumina and ceria-zirconia supports was indicated by the profile of the Rh K-edge white line and post-edge region of the XANES spectra, which could be correlated back to the presence of RhO_2-like species in the case of Rh/CeZrLa-Al_2O_3 while Rh_2O_3-like species seem to be dominant on the alumina support. Nonetheless, due to the well-known interaction of Rh with both CeO_2 and Al_2O_3, [8,50,51] the small variations in the XANES region in comparison to the spectra obtained for the reference oxides suggest a slight distortion of the rhodium local environment. The high dispersion of Rh species on both

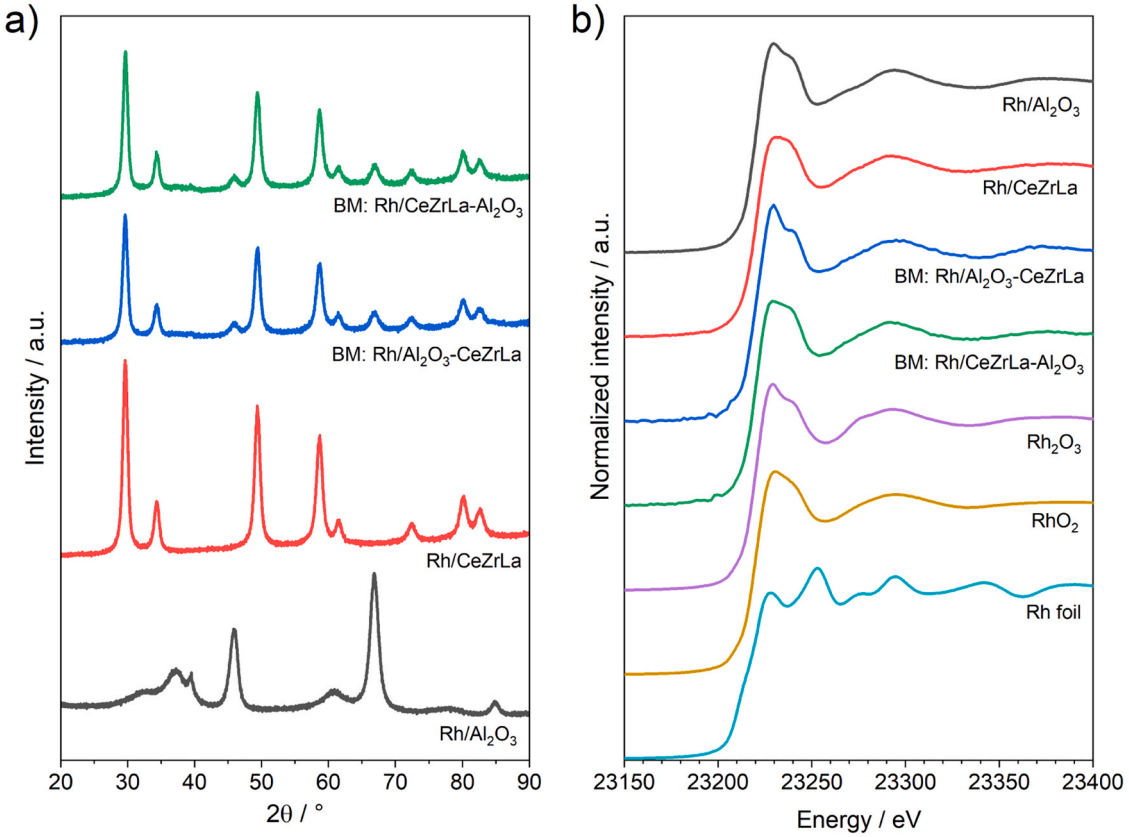

Fig. 1. a) XRD patterns of the Rh/Al_2O_3, Rh/CeZrLa, BM:Rh/Al_2O_3-CeZrLa and BM:Rh/CeZrLa-Al_2O_3 catalysts and washcoats; b) corresponding XANES data obtained at the Rh K-edge for the as prepared samples.

supports was also indicated by the corresponding FT-EXAFS data (Fig. S2), which showed contributions only in the first coordination shell around Rh atoms. However, despite it cannot be completely ruled out, the incorporation of Rh as substituted Rh^{3+} species in the CeO_2-ZrO_2 lattice or the exclusive formation of single sites could not be identified in the freshly prepared samples. A similar phase composition was found for the washcoats prepared by manual mixing (Figs. S1 and S2).

According to the HAADF-STEM (Fig. 2) and EDXS investigations (Fig. S3), Rh was present as highly dispersed entities with sub-nanometer size in the sample supported on CeZrLa (evaluation of size distribution not possible due to the high dispersion), and as small nanoparticles with a mean size of ~ 0.9 nm in the Rh/Al_2O_3 catalyst. The highly dispersed state of Rh on CeZrLa confirms the strong interaction with the support, in line with previous studies on comparable ceria-supported catalysts [12,52,53]. The formation of small Rh_2O_3 nanoparticles in the alumina-supported catalysts during calcination at relatively low temperatures was as well reported in the literature for similar systems [15,17]. In agreement with the XAS data shown in Figs. 1b and S2, the location of Rh on the initial support material after the preparation of the CeZrLa-Al_2O_3 washcoats was confirmed also by electron microscopy measurements (cf. Fig. S3). Due to the higher surface area of the alumina support (141 m^2/g vs. 80 m^2/g of CeZrLa) and lower molar mass (molar ratio Al_2O_3: ZrO_2: CeO_2: La_2O_3 = 4.9: 2.6: 0.7: 0.1), the manual mixing of the two materials in a 1:1 weight ratio resulted in the formation of CeZrLa-rich regions on the alumina surface. Additionally, whereas highly dispersed Rh_2O_3 particles were present on the Al_2O_3 support in the BM:Rh/Al_2O_3-CeZrLa washcoat, Rh seems to be solely located on the CeZrLa-rich areas in the BM:Rh/CeZrLa-Al_2O_3 sample.

The comparison of the catalytic performance for CO, NO and C_3H_6 conversion under stoichiometric conditions during three consecutive light-offs to 500 °C, 800 °C and 950 °C is presented in Fig. 3 for the Rh/Al_2O_3, Rh/CeZrLa and the respective BM washcoats. More precisely, the temperatures for 10% (T_{10}), 50% (T_{50}) and 90% (T_{90}) conversion are used to assess catalyst efficiency. The as prepared Rh/Al_2O_3 catalyst exhibits a narrow temperature window (250–280 °C) for the complete oxidation of CO during the first light-off to 500 °C (Fig. 3a), which shifts towards lower temperatures during the second activity cycle. In this case, the reaction already sets off at ~175 °C (10% conversion) and reaches 90% conversion at ~218 °C. During the third light-off/light-out cycle, the activity improvement is less pronounced, with only ~10 °C decrease in the T_{50} temperature. The Rh/CeZrLa catalyst (Fig. 3b), on the other hand, was able to convert CO already around 165 °C (T_{10}) during the first light-off/light-out cycle, which is almost 100 °C lower as measured for the Rh/Al_2O_3 catalyst. This behavior is most probably due to the contribution of the noble metal-ceria perimeter sites that help at overcoming the CO self-inhibition effect [54–57]. In this regard, the incorporation of Rh ions into the CeO_2 lattice was reported to occur at low noble metal loadings, which leads to the distortion of CeO_2 lattice and is beneficial after catalyst pre-reduction for the low-temperature CO oxidation activity under lean reaction conditions [8]. A similar behavior of Rh single sites was reported by Garcia-Vargas et al. during CO oxidation in excess of oxygen [50]. In our study, a broadening of the temperature window was observed when Rh was located on the CeZrLa support, as in this case 90% CO conversion was only reached at 237 °C. Besides using stoichiometric reaction conditions, this trend could be also caused by the significantly higher gas flows applied during our tests in comparison to previous investigations.

During the second light-off, the difference between the reaction onset and complete conversion is as well pronounced for the CeO_2-ZrO_2 supported sample. 10% of CO is already converted at 162 °C but 90% conversion is only reached at 242 °C. Nonetheless, after the catalyst exposure to higher temperatures during the second light-off/light-out cycle to 800 °C, the temperature window for CO oxidation becomes

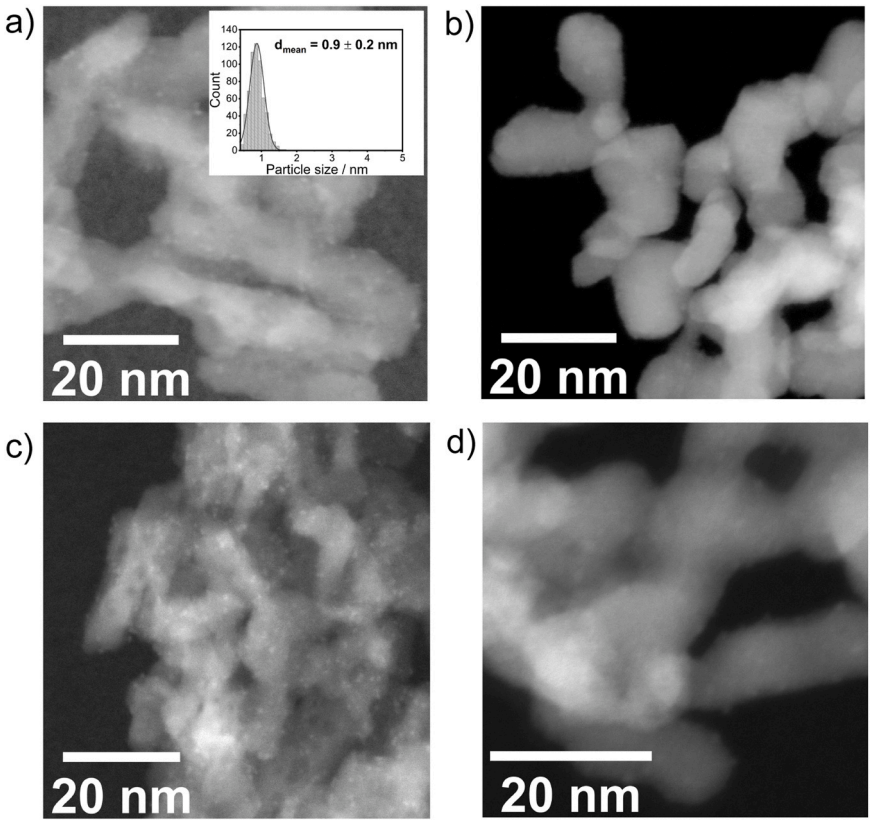

Fig. 2. HAADF-STEM images of a) Rh/ γ-Al_2O_3, b) Rh/CeZrLa, c) BM:Rh/γ-Al_2O_3+CeZrLa, d) BM:Rh/CeZrLa+γ-Al_2O_3 samples. Particle size distribution is shown for Rh/γ-Al_2O_3 catalyst, as obtained by evaluating 600 nanoparticles.

narrower, albeit at the expense of the low temperature conversion: T_{10} shifted to 176 °C, while 90% CO conversion was measured around 234 °C.

Due to the initial location of Rh on the alumina support, the BM:Rh/Al_2O_3-CeZrLa washcoat (Fig. 3c) exhibits a similar catalytic behavior as that observed for the Rh/Al_2O_3 catalyst, including a narrow temperature window and the improvement of the activity during consecutive catalytic cycles. Analogous, comparable CO oxidation activity was measured for the BM:Rh/CeZrLa-Al_2O_3 washcoat as for the Rh/CeZrLa catalyst, with a broad temperature window for CO conversion during all three light-off/light-out cycles while showing only minimal variations in the T_{10} and T_{90} temperatures (1st light-off: 176–240 °C; 2nd light-off: 177–237 °C; 3rd light-off: 178–232 °C).

Although for the oxidation of CO a significant difference in activity could be observed depending on the support type, the location of Rh on ceria or alumina does not seem to have a substantial impact on the NO reduction. All four samples featured similar conversion temperatures with minimal variations. Moreover, a comparable improvement in the catalyst activity was measured for both groups of samples over consecutive activity cycles. While the T_{50} temperature for NO reduction was measured around 320 °C during the first light-off, 50% of NO is converted already at 260 °C during the third light-off over Rh/Al_2O_3- as well as over Rh/CeZrLa-based catalysts. This behavior could be caused by the different mechanism of the NO reduction reaction, i.e. not involving the noble metal-support perimeter sites, but also due to the *in situ* structural evolution of Rh species reaching a similar state. Under the testing conditions applied in this study, comparable activity was measured also during the oxidation of C_3H_6 for the four samples investigated, with a slight improvement in propylene conversion after the first light-off/light-out cycle. However, if Rh is located on Al_2O_3 a more pronounced shift towards lower temperatures was observed than for the Rh/CeZrLa-based samples. In fact, despite the same trends being noticed irrespective of the initial support material, the Rh/Al_2O_3 catalyst as well as the Rh/Al_2O_3-based washcoat showed a better catalytic performance for the simultaneous conversion of CO, NO and C_3H_6 during the third catalytic cycle.

3.2. Dynamics in Rh state during catalytic cycles and fuel-cut ageing

To better understand the nature of the noble metal species and also how the noble metal-support interaction influences the catalyst evolution under reaction conditions, *operando* XAS measurements were conducted during several catalytic cycles and different ageing procedures (Scheme S1). As reported in the previous section, after the catalyst preparation Rh was present as small Rh_2O_3 nanoparticles on the alumina surface and as highly dispersed Rh^{4+} single atoms/clusters on the CeZrLa support (Fig. 1b). Fig. 4 reports the changes in the noble metal oxidation state derived by LCA of the *operando* Rh K-edge XANES data together with the corresponding CO, NO and C_3H_6 conversion profiles. During heating up to 500 °C in reaction mixture, the reduction of Rh species was observed to different extents for both catalysts. In line with the results of the laboratory tests, an earlier CO oxidation onset and complete conversion over a broader temperature window was measured during the *operando* XAS experiments for the Rh/CeZrLa-based sample (Fig. 4b). At the same time, only a slight reduction of Rh was noticed below 200 °C in this sample. In contrast, for the Rh/Al_2O_3 catalyst considerable CO conversion was measured only after the partial reduction of the noble metal species (about 30% reduced Rh, Fig. 4a). As mentioned previously, the observed difference is most likely caused by the role of the Rh-CeZrLa interface, which is known to actively contribute to oxidation reactions for various noble metal-based catalysts [54,55,57–59].

In contrast, the conversion of C_3H_6 and NO is reliant on the formation of metallic Rh species irrespective of the noble metal carrier. Sustained

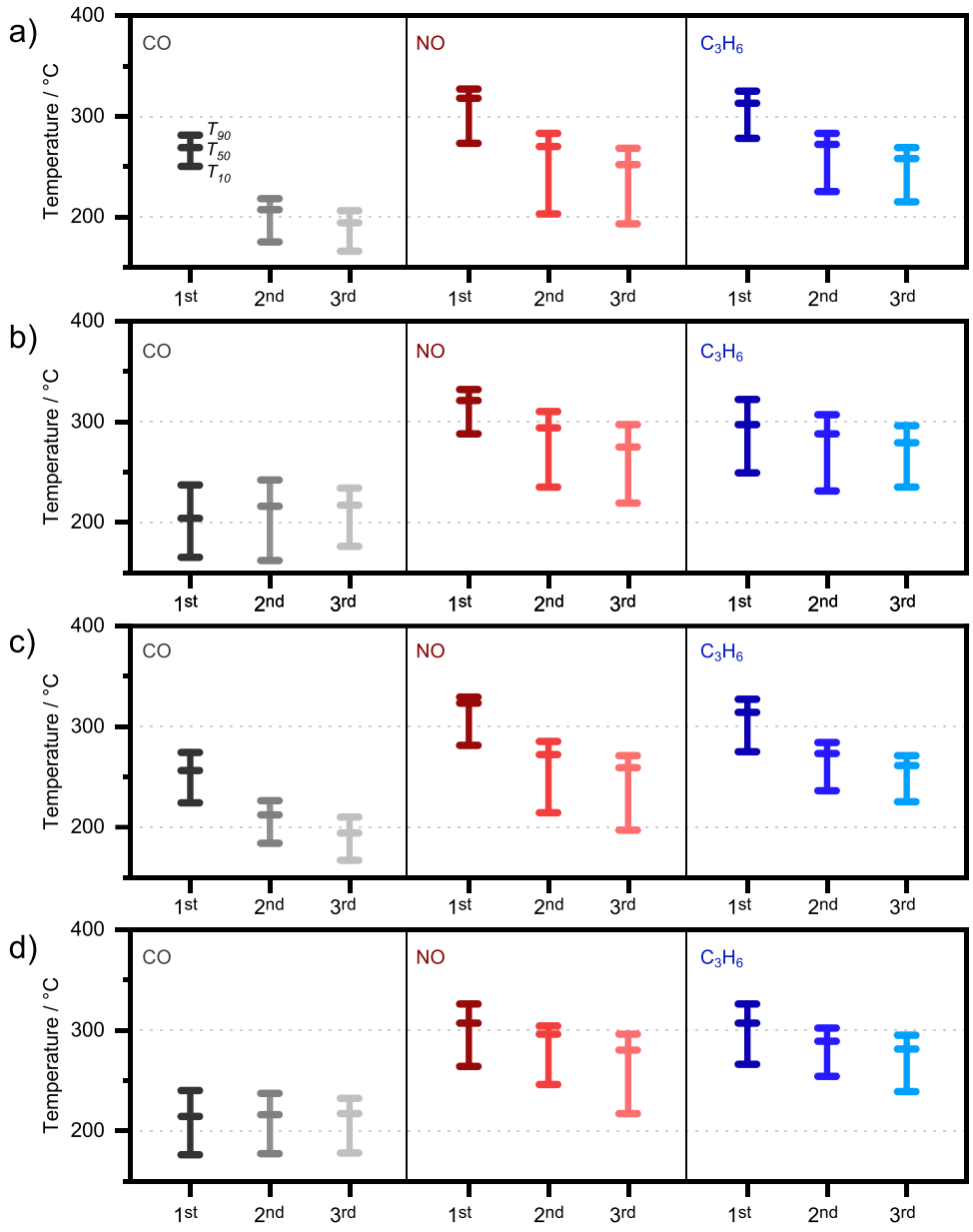

Fig. 3. Overview on the T_{10}, T_{50} and T_{90} temperatures measured for a) Rh/Al_2O_3; b) Rh/CeZrLa; c) BM:$Rh/\gamma\text{-}Al_2O_3$+CeZrLa; d) BM:Rh/CeZrLa+$\gamma\text{-}Al_2O_3$ during CO, NO and C_3H_6 conversion for three consecutive light-offs to 500 °C, 800 °C and 950 °C in a gas mixture containing 3000 ppm CO, 1000 ppm NO, 1000 ppm C_3H_6, 5400 ppm O_2 and 10% H_2O in N_2 (λ=0.998).

by the overall oxygen depletion due to CO and C_3H_6 oxidation, about 50% of Rh was in metallic state at 500 °C in the Rh/CeZrLa catalyst while almost complete reduction of Rh was found for the alumina-supported sample (90%). Also, in this case, the oxygen storage capacity of CeZrLa support combined with a stronger noble metal-support interaction in this temperature range most probably prevented a more substantial reduction of Rh species. During the reaction light-out, partial reoxidation was measured for the noble metal on the alumina support while almost complete reoxidation of Rh was found in the Rh/CeZrLa catalyst. These trends were maintained during the next light-offs to higher temperatures: complete reduction of Rh was observed for the Rh/Al_2O_3 catalyst above 600 °C while for the Rh/CeZrLa the metallic state was reached only above 900 °C. This different behavior is in line with previous studies on the interaction between Rh and alumina versus Rh and ceria-based supports depending on the temperature range and gas atmosphere: under O_2-rich conditions, Rh shows a stronger interaction with ceria at low temperatures while segregation and formation of separate RhO_x and CeO_2 phases occur at high temperature [12,53,60]. In contrast, the interaction of Rh with alumina was more pronounced at high temperatures in lean gas atmospheres [15], whereas the noble metal – support interplay seems to be prevented at low temperatures probably due to the OH groups present on the alumina surface. Hence, the more facile reduction of Rh on alumina under stoichiometric reaction conditions could be caused by the weaker noble metal-support interaction in the as prepared catalyst (i.e. calcination at 500 °C) in comparison to that exhibited by the less hygroscopic CeZrLa support.

After reaching 1000 °C during the subsequent activity light-off, the fuel-cut ageing conditions were simulated by periodic variations in the gas mixture between the stoichiometric reaction mixture and oxygen-rich atmosphere (each 15 min). In the presence of the O_2-rich atmosphere, complete reoxidation of Rh was noticed for the alumina-supported samples whereas less than 50% of Rh was reoxidized on the CeZrLa support (results of LCA of the Rh K-edge XANES data in Fig. 5a and b). Additionally, for Rh/Al_2O_3 the noble metal reduction extent

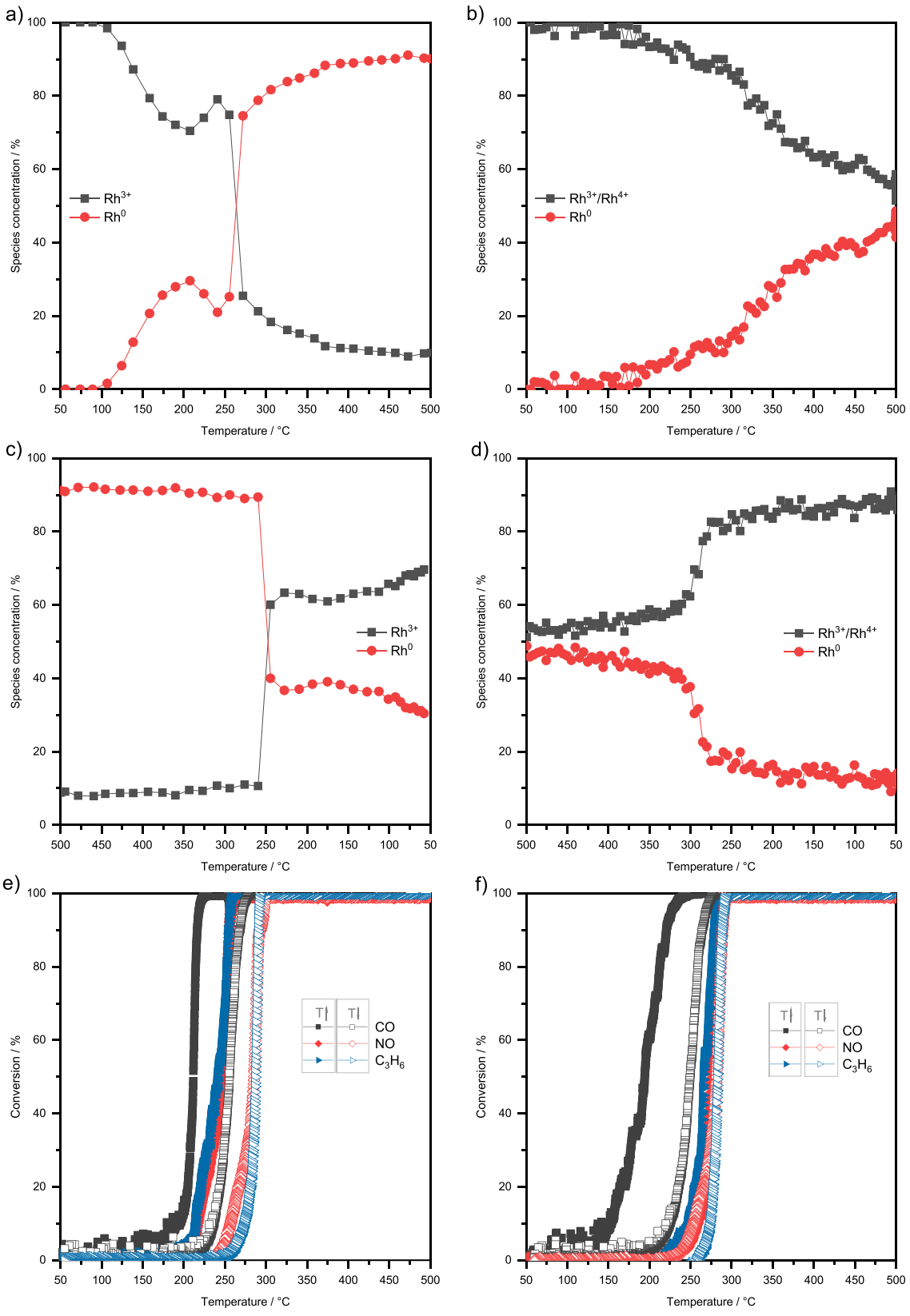

Fig. 4. Fraction of reduced (Rh^0, red circles) and oxidized (Rh^{3+}/Rh^{4+}, black squares – details in Fig. S2 c and d) species based on the LCA of the XANES data collected during the first light-off (a) Rh/Al_2O_3 and b) Rh/CeZrLa) and light-out (c) Rh/Al_2O_3 and d) Rh/CeZrLa) cycle to 500 °C with a heating rate of 10 °C/min. The corresponding conversion profiles of CO, NO and C_3H_6 are displayed in e) for the Rh/Al_2O_3 and f) for the Rh/CeZrLa catalysts. Gas mixture: 3000 ppm CO, 1000 ppm NO, 1000 ppm C_3H_6, 5400 ppm O_2 and 10% H_2O in N_2 (λ=0.998).

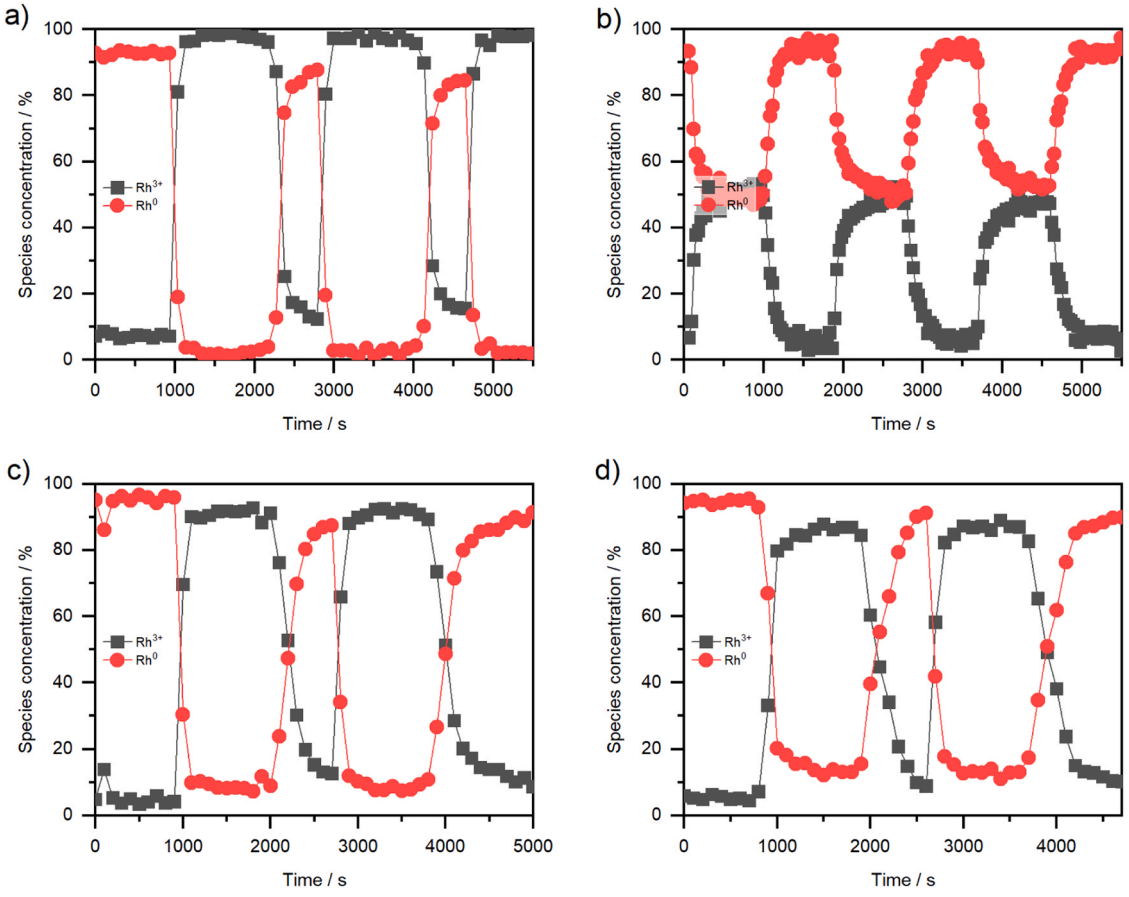

Fig. 5. FCA procedure at 1000°C for 1% Rh/Al_2O_3 (a), 1% Rh/CeZrLa (b), BM: Rh/Al_2O_3-CeZrLa washcoat (c) and BM: Rh/CeZrLa-Al_2O_3 washcoat (d). Six switches between reaction mixture and hydrothermal atmosphere with a duration of 15 min each were conducted.

diminishes over consecutive cycles while the oxidation level remains at 100%. On the contrary, the magnitude of Rh oxidation decreased in the Rh/CeZrLa catalyst during the fuel-cut procedure. Moreover, a steep noble metal oxidation step was noticed for the alumina-supported catalysts while the reduction of Rh species seems to be a slower process. For the CeZrLa catalyst, both redox steps are slow, indicating a different structural evolution at high temperature as well as a dissimilarity in the final steady state. These peculiarities of the noble metal behavior seem to clearly depend on the catalyst support. Accordingly, Rh species on alumina can be described as oxidized and highly stable entities that are difficult to reduce whereas the limited interaction of the noble metal with the CeZrLa support appears to lead to the formation of large metallic Rh particles that are slowly responding to the change in gas atmosphere. In line with these assumptions, the diffusion of Rh into the alumina surface/bulk with the formation of $RhAlO_x$-like species has been previously claimed by different research groups [15–17,21] while the sintering of rhodium oxide/metallic nanoparticles on ceria has been as well reported in several studies above 800 °C [12].

A similar profile of Rh reoxidation and reduction during the fuel-cut procedure as observed for the Rh/Al_2O_3 catalyst was also recorded for the BM:Rh/Al_2O_3-CeZrLa washcoat (Fig. 5c). Interestingly, even for the BM:Rh/CeZrLa-Al_2O_3 washcoat, the redox response of Rh species was analogous to that shown by the Rh/Al_2O_3 catalyst (Fig. 5d). Only a slightly faster reduction of the noble metal was observed for the BM:Rh/CeZrLa-Al_2O_3 washcoat. These differences indicate a distinct state of the noble metal in all Al_2O_3-containing samples in comparison to that present in the unmixed Rh/CeZrLa catalyst. This behavior could be triggered by the larger size of Rh particles on the CeZrLa support in comparison to those formed in the alumina-based materials at high temperatures. By assuming a higher mobility of the noble metal species with increasing temperature, the presence of RhO_x on the ceria-zirconia surface over a broader temperature window (light-off, Fig. 4) is expected to lead to an earlier sintering due to the lower melting point of rhodium oxides in comparison to the metallic Rh. On the other side, the lower surface area of CeZrLa promotes the growth of the noble metal particles as well irrespective of Rh oxidation state. In contrast, the spatial separation of the Rh/CeZrLa spots (Figs. 2c and S3) achieved during the ball milling with the Al_2O_3 support seems to prevent the strong sintering of Rh particles, maintaining their high redox activity, as previously demonstrated by Gashnikova et al. for analogous Pd-CeO_2/Al_2O_3 systems [6].

After the first fuel-cut ageing (1st FCA) procedure at 1000 °C, all samples were cooled in reaction mixture to room temperature. This step was followed by a second fuel-cut cycle (2nd FCA) and cooling in an oxygen-rich atmosphere (Scheme S1). The change of the gas atmosphere during the cooling step was done to accurately evaluate the state of Rh at the end of the O_2-rich step as well as the effect of temperature variation during catalyst ageing [61,62]. The comparison of the evolution of the noble metal state during the two fuel-cut ageing steps at 1000 °C is shown in Fig. S4. Both catalysts display a slightly more facile reduction of Rh species during the 2nd FCA procedure whereas the reoxidation step was less affected. Additionally, higher NO emissions were measured for the BM:Rh/Al_2O_3-CeZrLa washcoat during the 2nd FCA, which indicates an evolution in the catalyst state.

Accordingly, the XAS measurements conducted at room temperature at the end of the two experimental protocols revealed different noble metal states: Rh remained mostly in a reduced state after the 1st fuel-cut procedure and light-out under stoichiometric gas mixture whereas an oxidized state was identified for all samples cooled under hydrothermal conditions (2nd FCA, Figs. S4 and S5). This is pointed out by the results

of the LCA analysis of the XANES spectra and the FT-EXAFS data reported in Fig. 6 for the fresh and differently aged catalysts and washcoats. As a result of the 1st fuel-cut ageing at 1000 °C and cooling in reaction mixture, about 78% of Rh was present as metallic species in the Rh/Al_2O_3 catalyst whereas only metallic Rh nanoparticles were found in the Rh/CeZrLa catalyst at the end of the procedure. In fact, these states were generated at high temperatures upon the final switch to the reaction mixture and no further variation was observed during cooling. Only a slight reoxidation of the noble metal was noticed in Rh/Al_2O_3 around 300 °C (about 3%), which represents the temperature of reaction extinction. The evolution of the noble metal state during cooling after the 1st and 2nd FCA and the following light-offs is illustrated for Rh/Al_2O_3-CeZrLa washcoat in Fig. S5. After light-out in reaction mixture about 85% metallic Rh was found in this sample whereas 90% Rh^0 was present in the complementary Rh/CeZrLa-Al_2O_3 washcoat. The formation of noble metal nanoparticles was confirmed by the FT-EXAFS data collected at room temperature for all samples by the appearance of the Rh-Rh coordination sphere around 2.36 Å (Fig. 6).

In contrast, the prominent presence of the Rh-O coordination sphere around 1.56 Å for all samples after the 2nd fuel-cut step and cooling down in oxygen-rich atmosphere could be linked to the formation of oxidized Rh species during this ageing protocol. As shown for the Rh/Al_2O_3-CeZrLa washcoat in Fig. S5c, Rh oxidation occurs at 1000 °C and is maintained during cooling. However, solely for the Rh/CeZrLa catalyst, the Rh-Rh coordination sphere was still clearly visible in the FT-EXAFS spectra (Fig. 6c), also suggesting the presence of slightly larger nanoparticles in this catalyst that are only partially oxidized during cooling in oxygen, in line with the HAADF-STEM and EDXS data reported in Figure S6. In fact, the presence of partially reduced Rh particles in this sample at the end of the 2nd FCA procedure was also confirmed by the results of the fitting of the experimental EXAFS data (*k* range: 3–12 Å-1, R range: 1.2–3.2 Å) in R space (*k* weighting=3), which are reported in Table S7. In comparison, by mixing the CeZrLa–based catalyst with Al_2O_3 in the Rh/CeZrLa+γ-Al_2O_3 washcoat, the strong sintering of the noble metal particles seems to be prevented, as revealed by the lower intensity of the second coordination sphere after the 2nd FCA step (Fig. 6d). Hence, the evolution of Rh species during the light-outs/cooling steps was markedly different in both washcoats in comparison to Rh/CeZrLa, which is consistent with their different redox response during the fuel-cut cycles at 1000 °C (Fig. 5).

The catalytic activity data collected during the *operando* XAS measurements indicates only small effects of the 1st FCA procedure on the CO, NO and C_3H_6 conversion curves of the unmixed catalysts (Fig. 7a, b and e). A similar tendency was observed for the Rh/γ-Al_2O_3+CeZrLa and Rh/CeZrLa+γ-Al_2O_3 washcoats (Fig. 7e). Nonetheless, while an increase in the T_{50} was detected for the Rh/CeZrLa-based samples, a slight improvement in activity was noticed for the Rh/γ-Al_2O_3 based catalysts. For the unmixed Rh/CeZrLa sample, mostly the CO oxidation reaction is affected (ΔT = 27 °C), whereas the C_3H_6 (ΔT = 32 °C) and NO (ΔT = 25 °C) conversions are shifted towards higher temperatures over the Rh/CeZrLa+γ-Al_2O_3 washcoat. For the alumina-supported catalysts, almost an opposite trend was noticed, with comparable variations in the NO and C_3H_6 conversions but occurring at lower temperatures. Besides the reduction of the noble metal during the light-off (Fig. 4), the observed structural variations further indicate the presence of additional catalyst restructuring phenomena, which are dependent on the Rh-Al_2O_3 and Rh-

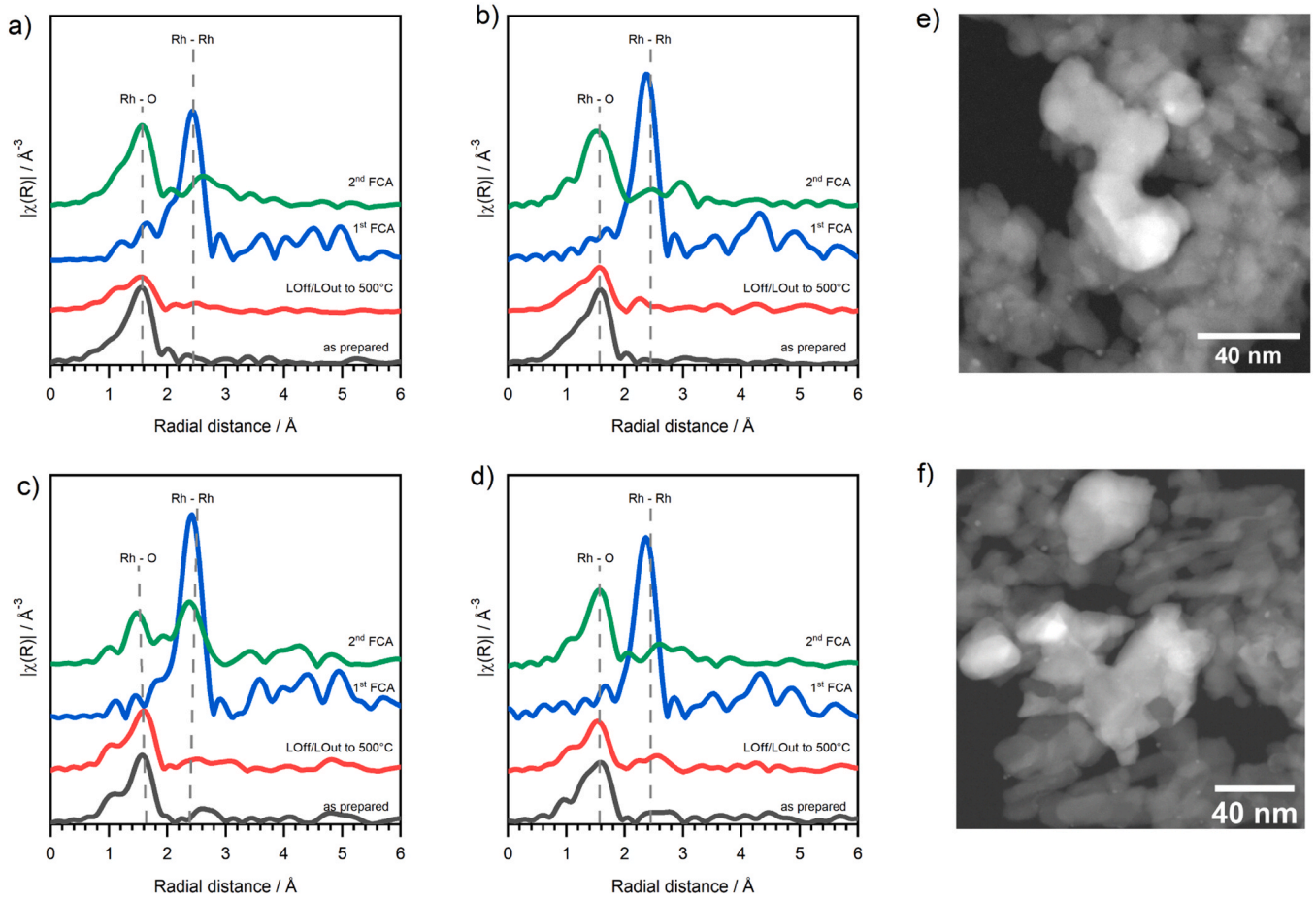

Fig 6. k^2-weighted FT-EXAFS data collected at 25 °C in He for Rh/γ-Al_2O_3 (a), BM:Rh/γ-Al_2O_3+CeZrLa (b), Rh/CeZrLa (c) and BM:Rh/CeZrLa+ γ-Al_2O_3 (d) after different stages of the *operando* XAS protocol (data not corrected for phase shift); HAADF-STEM images of BM:Rh/Al_2O_3-CeZrLa (e) and BM:Rh/CeZrLa-Al_2O_3 (f) washcoats at the end of the *operando* XAS measurements involving the 1st and 2nd FCA, and a light-off/light-out cycle to 800 °C.

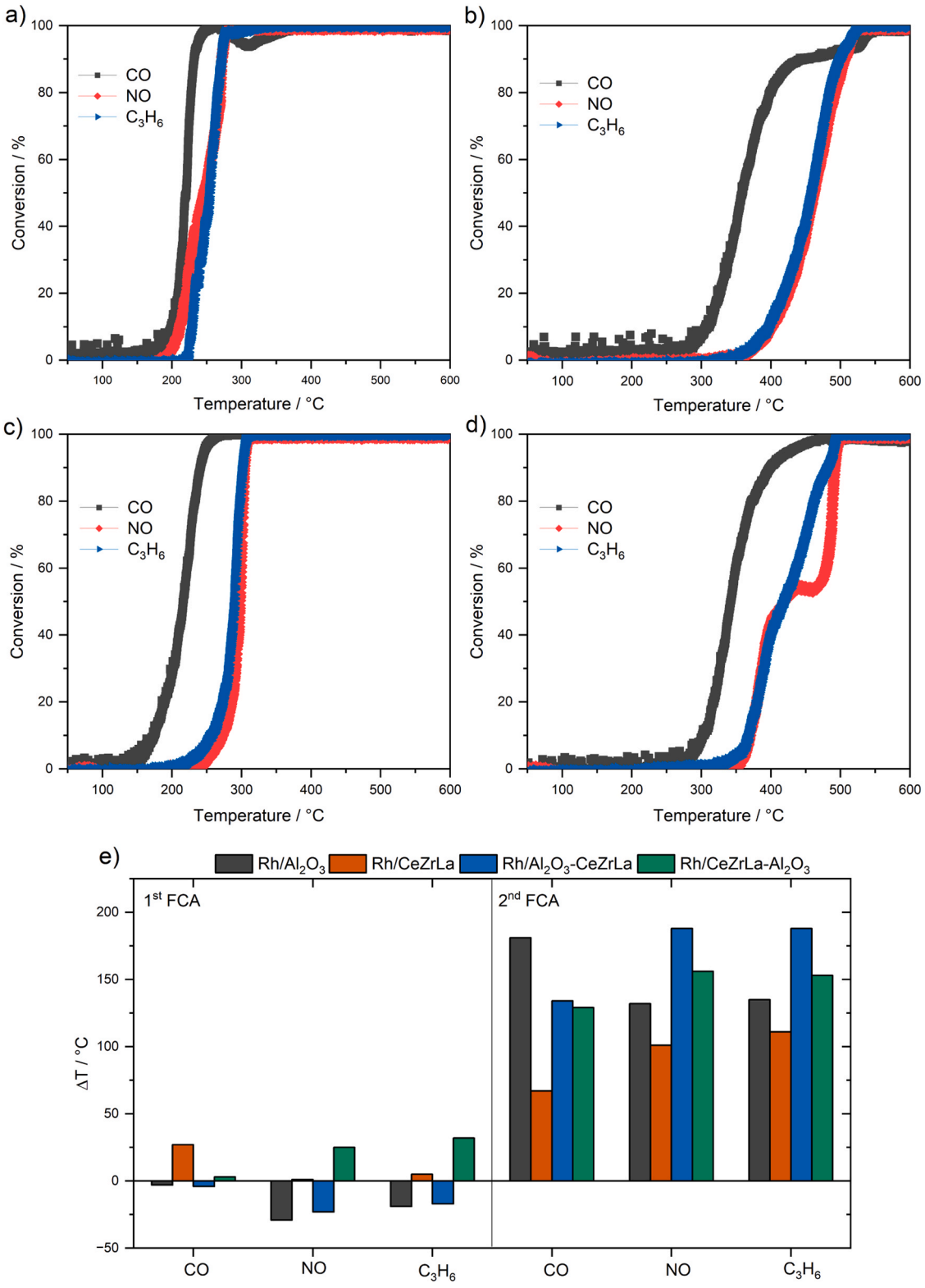

Fig. 7. Light-off activity data recorded during the *operando* XAS measurements for the BM:Rh/γ-Al_2O_3+CeZrLa (a, b) and BM:Rh/CeZrLa+ γ-Al_2O_3 (c, d) after the 1st and 2nd FCA procedures, respectively. Overview on the T_{50} variations upon ageing for the unmixed catalysts and washcoats (e): ΔT represents the difference between the T_{50} recorded for the fresh catalysts and that measured after different catalyst ageing steps.

CeZrLa interactions. In this regard, the *operando* XAS investigations reported above illustrate a distinct redox response during the FCA steps (Fig. 5) as well as a different noble metal particle size in the two unmixed catalysts (Fig. 6). Herein, the more pronounced sintering of Rh particles (higher intensity of the Rh-Rh contribution in the FT-EXAFS spectra after the 1st FCA, Fig. 6b) combined with a diminishment in the number of noble metal-support perimeter sites could explain the decrease in the CO oxidation activity for Rh/CeZrLa. For the BM:Rh/CeZrLa+γ-Al_2O_3 washcoat, the initial spatial confinement of Rh seems to help maintain a higher noble metal dispersion during the rather short FCA procedure at

1000 °C (slightly lower intensity of the Rh-Rh feature, Fig. 6d), which is in line with the smaller variation of the CO oxidation activity. On the whole, the formation of noble metal nanoparticles in reduced state after the 1st FCA seems to be beneficial for the alumina-supported catalyst and BM:Rh/γ-Al_2O_3+CeZrLa washcoat.

In contrast, the exposure to an oxygen-rich atmosphere during the cooling step from 1000 °C to 50 °C resulted in a pronounced catalyst deactivation for all samples investigated in this study. During the following light-off/light-out cycle, especially the alumina-based samples showed a shift of the CO oxidation light-off of about +181 °C or +134 °C for Rh/γ-Al_2O_3 and BM:Rh/γ-Al_2O_3+CeZrLa, respectively. Additionally, the CO conversion profile over the BM:Rh/γ-Al_2O_3+CeZrLa sample seems to be affected by the concurrent propylene steam reforming reaction between 400 – 500 °C due to the slightly rich reaction conditions (λ = 0.998). An increase of the T_{50} temperature for both NO and C_3H_6 conversions of +188 °C was also measured for the BM:Rh/γ-Al_2O_3+CeZrLa washcoat. At the same time, only a slightly lower deactivation extent was displayed by the BM:Rh/CeZrLa-γ-Al_2O_3 washcoat, with an increase of the conversion temperature of approximately +129 °C, +156 °C and +153 °C for CO, NO and C_3H_6, respectively. The impact of the CeZrLa support on the catalyst stability is more visible in the performance of the unmixed Rh/CeZrLa sample after the 2nd FCA. In comparison to the fresh catalyst state, the T_{50} temperature varied in this case only by +70–110 °C (ΔT) during the conversion of CO, NO and C_3H_6, which is still a larger difference than that observed after the 1st FCA.

To decode the evolution of the noble metal state during the two ageing procedures in the catalyst washcoats, HAADF-STEM images and EDXS maps were collected for the BM:Rh/γ-Al_2O_3+CeZrLa and BM:Rh/CeZrLa-γ-Al_2O_3 samples at the end of the *operando* XAS experiments (Fig. S6). For both washcoats, the good distribution of the CeZrLa islands on the alumina support obtained by ball milling was maintained during the fuel-cut ageing procedures. On the other hand, Rh nanoparticles with a mean size below 5 nm were observed all over the two CeO_2-Al_2O_3 mixed supports, despite the rather short ageing protocol. The fingerprint of their initial location was indicated only by the higher number of Rh nanoparticles present on Al_2O_3 in the fuel-cut aged BM:Rh/γ-Al_2O_3+CeZrLa sample. This development of the catalyst structure could be explained by the enhanced mobility of Rh species at high temperatures once the noble metal-support interaction is diminished. Especially, during the catalyst exposure to stoichiometric or slightly rich gas mixtures, the sintering of the metallic Rh particles is anticipated (state after FCA-1 procedure, Fig. 6) via movement and coalescence [10,63]. During this episode, the migration of Rh from one support to another is expected to occur. This behavior of Rh under reducing conditions was recently indicated also by the study of Machida et al. [14,64]. Nonetheless, possibly due to the different preparation of the catalyst washcoats (high excess of Rh/CeZrLaNd vs. γ-Al_2O_3) and ageing procedure (switches between stoichiometric/lean/fuel-rich gas mixtures at 1000 °C [64]), the encapsulation of Rh by CeZrLa support was not observed during our study. For mechanically mixed CeZrLa and Al_2O_3 based washcoats, the migration of Rh was suggested by Tomida et al. [37] to occur in both directions during 10 h hydrothermal ageing. At the same time, the formation of a separate RhO_x phase and pronounced sintering has been reported to take place on ceria under O_2-rich conditions [12,14], whereas Rh was shown to strongly interact with the alumina support at such high temperatures [21]. In spite of this, the homogeneous distribution and relatively small size of Rh nanoparticles at the end of the two FCA procedures do not align with an exclusive surface migration and growth mechanism of Rh particles.

According to the *operando* XAS results, in both washcoats Rh was completely oxidized in lean atmosphere and its reduction becomes more difficult during the consecutive fuel-cut cycles at 1000 °C. Furthermore, while on the pure CeZrLa support the formation of larger noble metal nanoparticles was indicated by the limited redox response during the FCA steps (Fig. 5b) and the *operando* FT-EXAFS characterization (Fig. 6b), a completely different behavior was noticed for the noble metal species in the two washcoats (Fig. 5c and d). As illustrated in Fig. 6 c and d, in this case the formation of metallic nanoparticles or partial reduction of Rh takes place during cooling down in reaction mixture (after FCA-1) and also during the last step of the experimental procedure (light-off between RT-800 °C after FCA-2). Considering the rather small size of the resulting noble metal nanoparticles at the end of the FCA-2 procedure combined with their fairly homogeneous distribution over the two metal oxide supports, the relocation and structural evolution of Rh during the fuel-cut cycles at 1000 °C most probably involves also the vapor phase migration during the oxygen exposure steps, which was previously shown to occur at such high temperatures [65].

3.3. Structural evolution and related effects of long-term hydrothermal ageing for Rh-γ-Al_2O_3 and Rh-CeZrLa-based washcoats

To estimate the influence of the vapor phase migration of Rh species from the ceria support to alumina under oxygen-rich conditions, the two BM washcoats were aged under hydrothermal ageing conditions at temperatures of 950 °C and 1050 °C for 12 h. These higher temperatures were selected considering the additional increase in the temperature of the catalyst bed that can occur during lambda variations due to the reaction exothermicity when switching to oxygen-rich conditions [66,67]. In the first step, hydrothermal ageing was applied at 1050 °C to the as prepared BM washcoats as well as to two analogous washcoats obtained by manual mixing of the catalyst powders and supports with a spatula (denoted MM, results reported in Fig. S19). The resulting tight (BM) or loose (MM) contact between the alumina and ceria counterparts allowed to further assess the contribution of the vapor phase migration beside the surface mobility of Rh species during catalyst deactivation. Finally, this comparison captures the influence of different washcoat preparation methodologies, which might lead to varying interparticle distances among the catalyst components.

Fig. 8a reports the CO, NO and C_3H_6 conversion measured for the hydrothermally aged BM washcoats during consecutive light-off/light-out cycles to 800 °C. Very similar trends were recognized for the BM Rh/γ-Al_2O_3+CeZrLa and Rh/CeZrLa+γ-Al_2O_3 washcoats, with pronounced deactivation measured during the first light-off, irrespective of the initial location of Rh species. For both samples the reduction of NO occurred between 430 °C and 510 °C whereas C_3H_6 oxidation was observed between 380 °C and 490 °C. An analogous decrease in activity was observed for the manually mixed washcoats during the first light-off after hydrothermal ageing (Figure S19a). In line with the results reported above, the active catalyst state was regained after the first light-off/light-out cycle to 800 °C. As illustrated in Fig. S6 for the Rh/γ-Al_2O_3+CeZrLa washcoat, the reactivation is due to the reduction of Rh species above 300 °C. However, in contrast to the facile reduction of Rh in the fresh Rh/γ-Al_2O_3 catalyst (Fig. 4), the high stability gained due to the strong interaction with alumina led only to a partial reduction (50%) even at 800 °C. Nevertheless, this structural change resulted in a pronounced enhancement of the low-temperature activity. No further variations were noticed in the CO, NO and C_3H_6 conversions between the 2nd and 3rd light-off/light-out cycle, and comparable activity profiles were measured for the BM and MM washcoats.

Taking into account the important role of the oxygen storage capacity (OSC) in the TWC functionality [68–70] but also the direct influence of the noble metal state on the oxygen reactivity [71], the impact of the hydrothermal ageing on the total OSC was evaluated during H_2-TPR experiments up to 950 °C in 10% H_2/Ar. Since the reduction of the noble metal species is expected to lead to the catalyst reactivation (Figs. S5 and 8), the first H_2-TPR test (1st TPR) was followed by catalyst reoxidation under mild reaction conditions (10% O_2/He up to 500 °C) and an additional H_2-TPR test (2nd TPR). To obtain a rough estimation of the total OSC for the HA and regenerated samples, this protocol was applied for both washcoats and also for the unmixed catalysts as references. The results reported in Fig. S20a indicate a significantly different

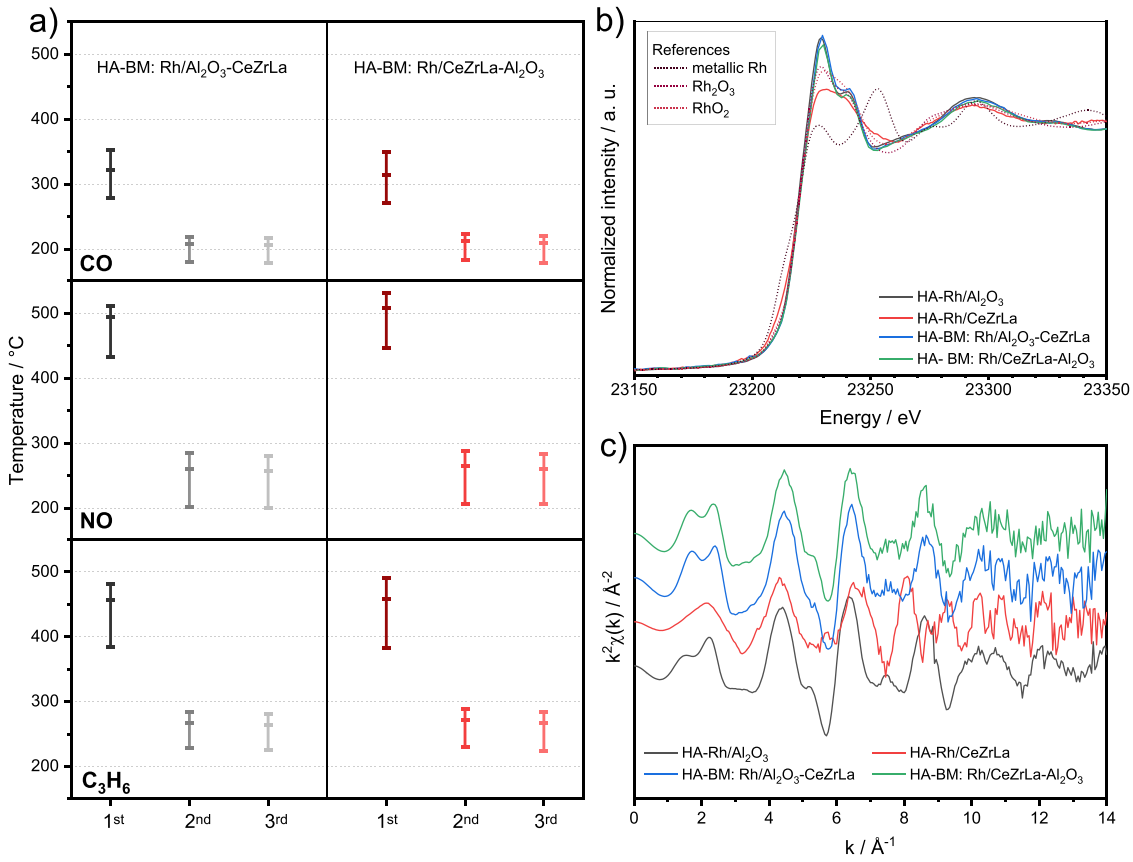

Fig. 8. Overview on the T_{10}, T_{50} and T_{90} measured for the hydrothermally aged BM: Rh/γ-Al_2O_3+CeZrLa and BM: Rh/CeZrLa+γ-Al_2O_3 washcoats during CO, NO and C_3H_6 conversion in three consecutive light-offs to 800 °C in a gas mixture containing 3000 ppm CO, 1000 ppm NO, 1000 C_3H_6, 5400 ppm O_2 and 10% H_2O in N_2 under stoichiometric conditions (a); Rh K-edge XANES (b) and EXAFS (c) data obtained for hydrothermally aged BM Rh/γ-Al_2O_3+CeZrLa and Rh/CeZrLa+γ-Al_2O_3 washcoats.

behavior for the two HA-Rh/γ-Al_2O_3 and HA-Rh/CeZrLa catalysts. For the CeZrLa supported sample, the reduction of Rh particles occured below 200°C, and was followed by the reduction of the CeZrLa support at higher temperatures [72]. The two peaks appearing at lower temperatures have been previously assigned by Fornasiero et al. [73] to the reduction of Rh_2O_3 particles with a non-uniform size. These features were not visible for the HA-Rh/γ-Al_2O_3, which displayed the onset for the reduction of Rh species above 200 °C. Furthermore, this process was not completed even at the highest temperature of the H_2-TPR experiment. For the HA-Rh/γ-Al_2O_3+CeZrLa and HA-Rh/CeZrLa+γ-Al_2O_3 washcoats, an almost identical reduction profile was recognized. Only a slightly higher total H_2-consumption was measured for the washcoat with Rh initially located on the CeZrLa support (11.64 ml/g_{cat} vs 10.06 ml/g_{cat}, Table S6). First of all, the low temperature reduction peak that appeared for the unmixed HA-Rh/CeZrLa catalyst was not present anymore. Only the H_2-consumption peak around 170 °C was followed by the CeZrLa reduction peak at ~260 °C. The disappearance of the first peak and the small shift of the second one relative to the HA-Rh/CeZrLa catalyst indicate a structural change and further stabilization of Rh species. At the same time, the reduction of CeZrLa at slightly lower temperatures could be caused by the formation of small CeZrLa patches on the alumina support during the ball milling, which prevented a more severe sintering of CeZrLa particles. This trend is in line with previous studies on the redox behaviour of similar CeO_2-ZrO_2/Al_2O_3 supports [74].

After the mild reoxidation of the samples at 500 °C, the results of the 2nd H_2-TPR experiment suggest at least the partial recovery of Rh species in all samples. For the HA-Rh/γ-Al_2O_3 catalyst, weak reduction peaks are visible around 76 °C and 230 °C (Figs. S19 b and d). Significantly less pronounced as observed during the 1st TPR experiment, H_2-consumption was still noticed for this catalyst above 350 °C, which could hint to the simultaneous presence of highly stable Rh species. This state is in line with the evolution of the Rh redox response during the fuel-cut ageing (Fig. 5) and indicates that 950 °C might not be sufficiently high for the complete recovery of Rh species under transient H_2-TPR conditions (1st run). For the unmixed HA-Rh/CeZrLa catalyst, the reduction of Rh below 100 °C occurred almost simultaneously with the reduction of CeZrLa. Only a slight H_2-consumption step was noticed above 250 °C, which could be caused by the reduction of bulk CeZrLa. This trend is explained by the presence of highly dispersed and redox active Rh species in the fresh Rh/CeZrLa-bases samples in comparison to the sintered Rh particles formed at high temperature during the fuel-cut aging. Hence, a similar behavior was displayed by the two washcoats; although a broader H_2-consumption peak was measured for HA-Rh/γ-Al_2O_3+CeZrLa and HA-Rh/CeZrLa+ γ-Al_2O_3 washcoats in comparison to the unmixed catalyst (several components in the deconvoluted H_2-TPR data, Fig. S21) the earlier reduction of CeZrLa is probably promoted by the rather homogeneous distribution of Rh particles that was induced during the HA procedure (Figs. 6e and f) and also during the 1st TPR step.

On the other hand, this pronounced change in the redox response of CeZrLa has been previously reported to occur as a consequence of ageing or redox treatments at high temperatures. Despite the decrease of the specific surface area (in this study from 80 m^2/g to 43 m^2/g for the HA-Rh/CeZrLa catalyst), the variation of the lattice parameters or the formation of the $CeZrO_4$ κ-phase were formerly correlated with this increased oxygen mobility [73,75–78]. The overall H_2 consumption reported in Table S6 is higher for the HA-Rh/CeZrLa catalyst during the

1st H_2-TPR test (31.8 ml/g_{cat}) in comparison with that measured for the washcoats (10.1 ml/g_{cat} for HA-Rh/γ-Al_2O_3+CeZrLa and 11.6 ml/g_{cat} for HA-Rh/CeZrLa+γ-Al_2O_3) but decreases significantly during the 2nd TPR experiment (9.0 ml/ g_{cat}). This trend is probably due to the sintering of both NM particles and carrier material, with the later known to be accelerated under reducing conditions due to the formation of oxygen vacancies [79]. For the two washcoats, almost the same H_2-consumption was measured, which is also the highest among all samples during the 2nd TPR (11.1 ml/g_{cat} for HA-Rh/γ-Al_2O_3+CeZrLa and 10.1 ml/g_{cat} for HA-Rh/CeZrLa+γ-Al_2O_3). Also, in this case, the stabilization of CeZrLa in the washcoats probably prevents a severe sintering and explains the rather minor difference between the H_2-consumption measured during the two TPR experiments.

All in all, the resemblance in the redox response and catalytic activity of the different washcoats as well as their similar reactivation behavior suggest a comparable state of the noble metal species in these samples. To confirm this assumption, additional material characterization was conducted. The XRD patterns obtained for the hydrothermally aged washcoats display the phase transformation of γ-Al_2O_3 to θ-Al_2O_3 for all samples (Fig. S8a). XRD patterns corresponding to CeZrLa were as well identified but no characteristic reflections of oxidized or metallic Rh species were observed. The corresponding XANES (Fig. 8b) and FT-EXAFS spectra (Fig. S8b) at Rh K-edge indicate that Rh is present in all samples in an oxidized state. Moreover, the higher intensity of the white line in comparison with that of rhodium oxide references, points out a different local structure and coordination geometry. Besides the main Rh-O coordination shell in the FT-EXAFS, features previously assigned to the Rh-O-Rh and Rh-O-Al shells are visible around 3.45 Å and 2.87 Å, respectively [80]. Additionally, the *k*-space EXAFS spectra (Fig. 8c) of the aged washcoats show a high similarity with that obtained for the hydrothermally aged Rh/Al_2O_3 catalyst while a different profile was recorded for the Rh/CeZrLa sample after ageing. Distinct features at $k = 5.2$ Å^{-1}, $k = 7.5$ Å^{-1} and $k = 10$ Å^{-1} suggest the same local structure for Rh in the four washcoats, which indicates the possible formation of a $RhAlO_x$ composite [80]. In contrast, the formation of partially reduced Rh nanoparticles is pointed out by the XANES profile and the appearance of the Rh-Rh shell around 2.4 Å in the FT-EXAFS spectra of the pure Rh/CeZrLa catalyst after hydrothermal ageing at 1050 °C (Fig. S8b).

Considering the limitations of the FT-EXAFS analysis in distinguishing overlapping shells of different atoms, the wavelet transform (WT) [81] of the extended X-ray absorption fine structure was used to conclude on the local environment of Rh atoms before and after the different ageing procedures. This method is particularly powerful in differentiating neighbouring atoms with significantly different weights. More exactly, heavier atoms show their fingerprint at higher wavenumbers while the lighter elements contribute to lower wavenumbers. The results of the WT-EXAFS analysis for the as prepared Rh/Al_2O_3 catalyst and BM/MM Rh/Al_2O_3-CeZrLa and Rh/CeZrLa-Al_2O_3 washcoats (top) are depicted as 2D maps in Figs. 9 and S10 alongside those obtained for the hydrothermally aged catalysts (bottom). In all cases, the main lobe between 1.0–1.9 Å (R scale) and 3–11 Å^{-1} (*k* range) can be associated with the Rh-O contribution, based on the comparison with the WT-EXAFS maps derived for the Rh_2O_3 and RhO_2 references (Fig. S9). The broadening effect observed for low R-values towards higher k values is a limitation of the WT analysis, already previously reported in literature [82]. One additional small lobe can be distinguished for the fresh BM:Rh/γ-Al_2O_3+CeZrLa washcoat between 2.5 – 3 Å that could be due to the bonds with heavier atoms. Despite the neighbouring Rh atom in Rh_2O_3 is expected to contribute in the same spectral region (Fig. S9b), the low intensity of these features did not allow a clear assignment.

WT-EXAFS analysis reveals a clear impact of the ageing procedure on the structure of the noble metal species. While beforehand only oxygen neighbours could be identified as backscattering atoms, after the long-term ageing the contribution of heavier elements at higher *k* ranges was observed. This is illustrated by the new features emerging at ~2.2 – 3.4 Å / 4–10 Å^{-1}, which are also present for the hydrothermally aged Rh/Al_2O_3 catalyst (Fig. 9e) and could be induced by Al neighbors. To elucidate the local structure around Rh sites, DFT calculations were used to generate the coordination sphere of substituted Rh^{3+} species into the θ-Al_2O_3 (100) surface. Considering the phase transformation of γ-Al_2O_3 during the hydrothermal ageing (Fig. S8a), the substitution of Rh at the octahedrally coordinated Al sites into the θ-Al_2O_3 (100) surface, first subsurface and second subsurface layers were considered (see details in SI). Despite Rh nanoparticles were observed on CeO_2 upon ageing and Rh nanoclusters were present on γ-Al_2O_3 in the fresh samples, Rh single sites were selected as the most suitable structure for DFT calculations since such species are expected to form on alumina during catalyst ageing under O_2-rich atmosphere. The calculated DFT structures (Fig. S17) were used to derive the theoretical EXAFS spectra and the corresponding WT-EXAFS 2D maps. As shown in Figs. 9d, h and S11, all these structures display a lobe around 1.5 Å / 6 Å^{-1} in the first coordination sphere and two additional lobes between 2.4 and 3.5 Å / 4–10 Å^{-1}. For the second coordination sphere, the highest similarity with the experimental data is shown by the $RhO_{1.5}$ species substituted at octahedrally coordinated Al sites in the first subsurface layer, which is also the most energetically favorable position (Tables S3 and S5). This configuration is well matching the experimental data obtained for the hydrothermally aged Rh/Al_2O_3 (Fig. 9a) and the two HA washcoats (Fig. 9f and g) but not with the aged Rh/CeZrLa catalyst (Figure S10d). The corresponding structures of adsorbed and substituted noble metal species on the γ-Al_2O_3 (110), CeO_2 (111) and ZrO_2 (101) surfaces were as well evaluated (Figs. S16 and S17), but no resemblance could be found also considering the applied temperature range of the HA protocol. Overall, these results are in agreement with previous literature reporting the strong interaction between Rh and Al_2O_3 [17,21,83]. Moreover, the *ex situ* XAS measurements supported by the electron microscopy data demonstrate the migration of Rh under oxidizing conditions leading to the formation of $RhAlO_x$ composites also in the Rh/CeZrLa-Al_2O_3 washcoats, irrespective of the mixing procedure applied at their preparation, i.e. ball-milling or manual mixing.

To evaluate the extent of the noble metal transfer from the CeZrLa to the Al_2O_3 support, in an additional experiment the Rh/CeZrLa catalyst was spatially separated from the γ-Al_2O_3 in a plug-flow reactor, as illustrated in Table 1. In an analogous test, the Rh/γ-Al_2O_3 sample was positioned upstream and the CeZrLa support in the downstream position. Starting with bulk metallic Rh, the oxidation of Rh was observed mostly below 900–950 °C while above these temperatures the sublimation of RhO_x is expected [65,84]. Generally, the formation of gaseous RhO_2, RhO or even Rh_2O_3 was reported in literature to occur at high temperatures [65,85,86]. Based on this information, hydrothermal ageing was applied at both 950 °C and 1050 °C for the separated catalyst beds, which cover the typical temperature window of the fuel-cut ageing procedure [62,66]. After 12 h at 950 °C, ICP-OES analysis showed that the initial composition of the Rh/CeZrLa and Rh/Al_2O_3 samples was maintained (Table 1). On the contrary, the migration of Rh at 1050 °C was already indicated by the colorization of the alumina support, especially at the beginning of the catalyst bed, and brightening of the Rh/CeZrLa catalyst bed (Table 1). *Ex situ* XANES measurements at the Rh K-edge (Fig. 10) were conducted for the resulting 1050 °C / 12 h and 1050 °C / 24 h Rh/Al_2O_3 and Rh/CeZrLa samples. The obtained data confirmed the presence of Rh in an oxidized state on the Al_2O_3 support located downstream in the fixed-bed reactor. Moreover, the XANES profiles were very similar to those acquired for the two hydrothermally aged BM: Rh/CeZrLa-Al_2O_3 and Rh/Al_2O_3-CeZrLa washcoats (Fig. 8), confirming a similar state for the Rh species, but distinct in comparison to the bulk rhodium oxides.

Elemental analysis results validated as well the presence of Rh on the Al_2O_3, with a noble metal loading amounting to 0.04 wt% while no CeZrLa support traces could be identified. At the same time, Rh concentration changed from 0.8 wt% Rh in the fresh Rh/CeZrLa catalyst to

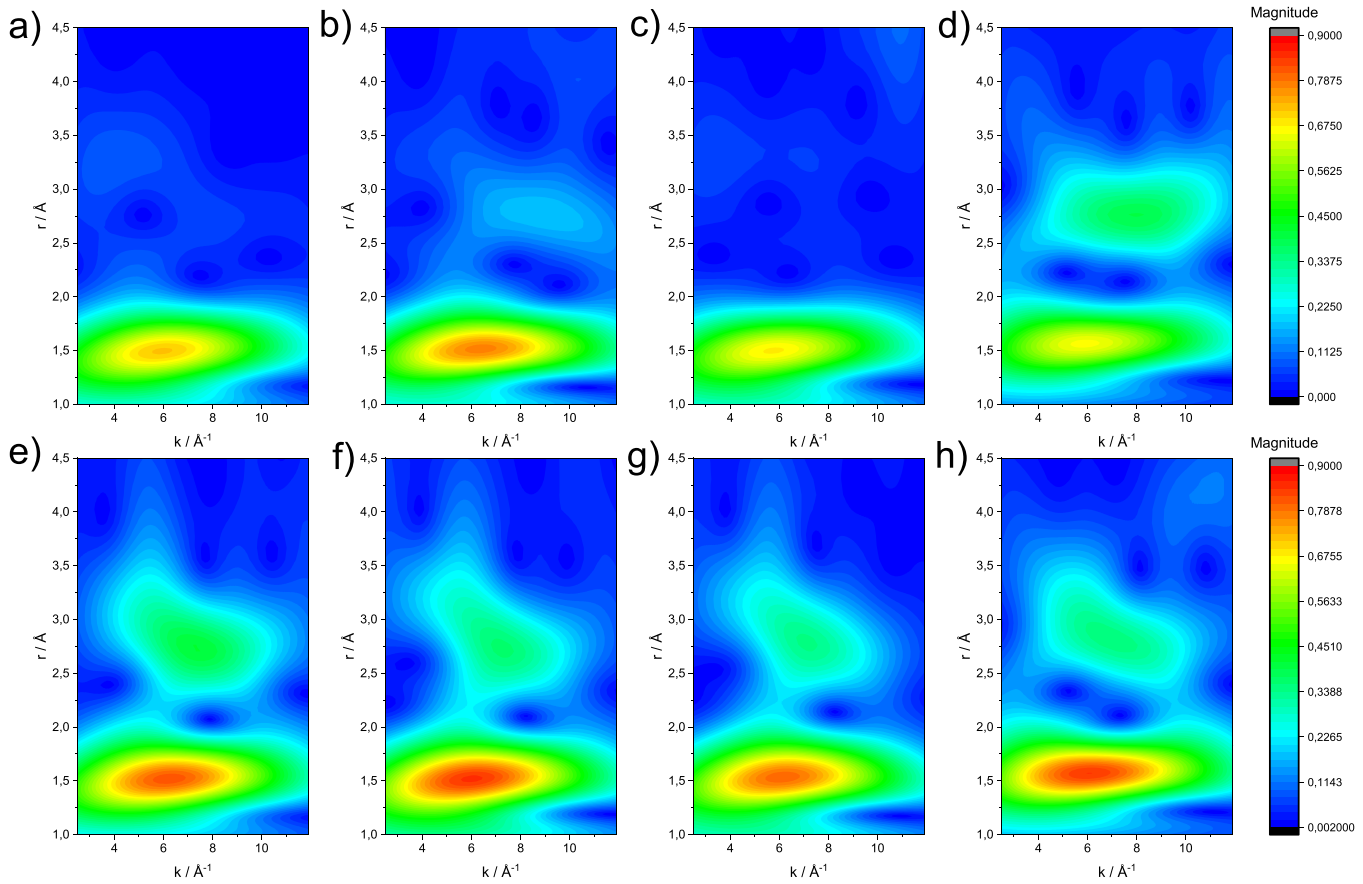

Fig. 9. WT-EXAFS data obtained for the fresh (top) and hydrothermally aged (bottom) catalysts and washcoats Rh/γ-Al_2O_3 (a,e), BM: Rh/γ-Al_2O_3+CeZrLa (b, f), BM: Rh/CeZrLa+γ-Al_2O_3 (c, g); Calculated WT-EXAFS maps of Rh/θ-Al_2O_3 containing octahedrally coordinated Rh in different layers of θ-Al_2O_3 (100) facet (based on DFT modeling): (d) surface layer, (h) first subsurface layer.

0.6 wt% after 12 h hydrothermal ageing at 1050 °C (Table 1). Despite a certain error bar needs to be considered, the observed trend indicates that a significant amount of Rh-volatile species bypassed the alumina grains during ageing. Extending the hydrothermal ageing at 1050 °C to 24 h, did not induce any further significant transfer of Rh to the alumina support. According to the ICP-OES results, ~0.61 wt% Rh was still present in the Rh/CeZrLa −1050 °C/24 h catalyst while Rh concentration amounted 0.08 wt% in the newly formed Rh/γ-Al_2O_3 −1050 °C/24 h sample. The same trend was identified after ageing separately the Rh/CeZrLa and Rh/γ-Al_2O_3 catalysts: a noble metal loss of around 54% for the CeZrLa supported sample and only about 6.6% variation for the alumina-based catalyst. This behavior suggests the stabilization/storage of part of Rh species on the alumina support. At the same time, either the stabilization of the remaining RhO_x by the CeZrLa support or the formation of slightly larger noble metal particles with a decreased oxidation/sublimation rate seem to occur in the Rh/CeZrLa sample. Partial reduction of the remaining Rh to metallic state on the CeZrLa support is indicated by the XANES profile obtained for these samples (Fig. 10) and also by the FT-EXAFS data reported in Fig. S8b for the HA-Rh/CeZrLa catalyst. However, the corresponding HAADF-STEM/EDXS investigations of the HA-Rh/CeZrLa sample mostly uncovered the presence of highly dispersed and uniformly distributed Rh subnanometer entities (Figs. S12). Additionally, the formation of Rh atom rafts-like with a preferential location on the CeZrLa support was noticed (Figs. S12e-g), as previously observed for Pt on CeO_2 [87]. Overall, this outcome implies that only a part of Rh species is stabilized by the interaction with the unmixed ceria-zirconia support while the rest is leaving the catalyst via the gas phase.

According to more recent studies [88,89], noble metal sintering is to a great extent prevented for noble metal loadings that correspond to a theoretical monolayer coverage on the support surface. To verify this possibility, the fraction of the theoretical monolayer concentration of Rh on the CeZrLa and Al_2O_3 supports in the fresh and hydrothermally aged catalysts (separately treated, Table S2) was estimated assuming the formation of Rh single sites. Based on DFT calculations, the size of the unit cell of Rh single sites substituted into the γ-Al_2O_3 (110) or θ-Al_2O_3 (100) surfaces was used to derive the monolayer occupancy depending on the Rh loading in the fresh and aged Rh/Al_2O_3 catalysts (details in SI and Table S3). The CeZrLa system is a much more complex system, and Rh can be additionally stabilized at surface defects/vacancies generated by the CeO_2-ZrO_2 lattice distortion and due to the La^{3+} doping. Moreover, the interaction of Rh with ZrO_2 was reported in literature [90,91], and the formation of $(RhO)_{ads}$ and $(RhOH)_{ads}$ species on the ZrO_2 (101) surface was proposed by Thang and Pacchioni [90]. Finally, the direct interaction with La cannot be excluded considering its rather high loading (10 wt%) and the possible formation of $LaRhO_3$ under oxidizing conditions [92]. A similar interaction with Rh was reported for Nd-doped three way catalysts [93]. However, by comparing the XANES profile obtained for the Rh/CeZrLa sample after hydrothermal ageing at 1050 °C for 12 h with an analogous aged sample supported on La_2O_3 (Fig. S13), it can be concluded that the interplay between Rh and La does not represent an exclusive path for Rh stabilization at these high temperatures. In this case, the concurrent role of CeO_2-ZrO_2 cannot be excluded, as also illustrated by the electron microscopy results reported in Fig. S12. Hence, to obtain a rough estimation of the surface fraction occupied by hypothetical Rh single sites on the CeZrLa support, we used the DFT calculated structures of Rh single sites on the CeO_2 (111) and ZrO_2 (101) facets, similarly as applied in reference [7]. Additionally, we

Table 1
ICP-OES results for the catalysts aged in a spatially-divided geometry: the granulated Rh/CeZrLa and γ-Al_2O_3 were spatially separated with a layer of quartz wool in a fixed-bed reactor with an outer diameter of 1 cm. Hydrothermal ageing was conducted between 950 °C-1050 °C in 20 vol% O_2, *10 vol% H_2O/N_2*. The unmixed samples were aged in a similar manner, at the middle position of the catalyst bed.

Sample	Position in reactor	Ageing temperature (°C)	Duration (h)	Rh loading (wt%)	Evolution of the catalyst bed for the configuration marked with grey
1 wt% Rh/CeZrLa	Beginning	950	12	0.88 ± 0.005	
γ-Al_2O_3	End	950	12	< 0.005	
1 wt% Rh/CeZrLa	Beginning	1050	12	0.60 ± 0.024	
γ-Al_2O_3	End	1050	12	0.04 ± 0.002	
1 wt% Rh/CeZrLa	Beginning	1050	24	0.61 ± 0.013	
γ-Al_2O_3	End	1050	24	0.08 ± 0.003	
1 wt% Rh/ γ-Al_2O_3	Beginning	1050	12	0.88 ± 0.004	
CeZrLa	End	1050	12	0.02 ± 0.001	
1 wt% Rh/ γ-Al_2O_3 (fresh)	-	-	-	0.82 ± 0.004	
HA-1 wt% Rh/γ-Al_2O_3	Mid	1050	12	0.76 ± 0.052	
1 wt% Rh/CeZrLa (fresh)	-	-	-	0.80 ± 0.005	
HA-1 wt% Rh/CeZrLa	Mid	1050	12	0.37 ± 0.009	
BM: Rh/γ-Al_2O_3 + CeZrLa (fresh)	-	-	-	0.45 ± 0.066	
HA - BM: Rh/γ-Al_2O_3 + CeZrLa	Mid	1050	12	0.46 ± 0.067	
BM: Rh/CeZrLa + γ-Al_2O_3 (fresh)	-	-	-	0.46 ± 0.067	
HA - BM: Rh/CeZrLa + γ-Al_2O_3	Mid	1050	12	0.47 ± 0.069	

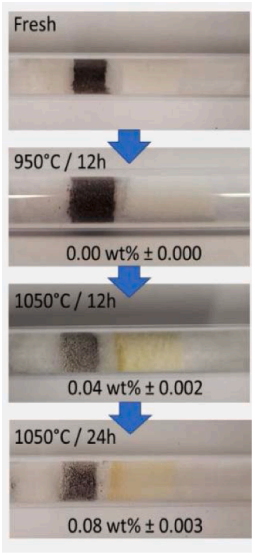

considered a mean size of the unit cell based on the CeO_2:ZrO_2 molar ratio in the CeZrLa support (details in SI). The results obtained for the fresh and hydrothermally aged Rh/γ-Al_2O_3 catalyst indicate a slight increase of the single site monolayer coverage from ~22.9% to 29.6%, which is due to the γ-Al_2O_3 to θ-Al_2O_3 phase transformation, smaller unit cell of Rh single sites and sintering of the support at 1050 °C. For the CeZrLa supported catalyst, the variation is similar but in the opposite direction: 29.6% monolayer coverage in the fresh sample at 0.8 wt% Rh loading while a fraction of 25.4% was estimated for the hydrothermally aged sample containing 0.37 wt% Rh. Hence, approximatively the same monolayer coverage is maintained after the catalyst ageing despite the noble metal volatilization and support sintering are implied. This behavior suggests that the unmixed CeZrLa support can stabilize the noble metal species even at this high temperature, i.e. 1050 °C, but only within a narrow concentration window that corresponds to about 25–30% of a theoretical single-site monolayer. Considering that our results do not indicate a preferential location of Rh at La-rich sites with the formation of mixed oxides (XANES data in Fig. S13) and also that this value exceeds the La loading in terms of monolayer coverage, the interaction of Rh with CeO_2 and ZrO_2 at different temperatures was evaluated by DFT calculations. The obtained phase diagrams of adsorbed and substituted RhO_x single site species on the CeO_2 (111) and ZrO_2 (101) facets are shown in Figs. S16 and S17. For comparison, the phase diagrams and the Bader charge vs. Rh oxidation state are shown for bulk Rh, Rh_2O_3 and RhO_2 reference systems in Figures S14 and S15. In both cases, the adsorbed RhO_x species are expected to escape from the single site locations already at low temperatures. While the substitution of a Ce atom in the CeO_2 surface by Rh does not generate a stable noble metal state, RhO_2 substituted species show a good stability on ZrO_2 but only up to 600 K (Fig. S17). However, since new defects/oxygen vacancies are generated in ceria-zirconia supports [69], the stabilization of a certain Rh fraction on CeZrLa at higher temperatures is probably linked to the remaining defects/vacancies on the support surface after hydrothermal ageing at 1050 °C.

In general, the ageing process leads to the increase of the surface noble metal concentration, which was shown to promote the formation of the noble metal particles [89]. The appearance of Rh aggregates is endorsed also by the lower number of anchoring sites for Rh on the sintered support (i.e. surface defects), as previously shown for Pt/CeO_2 catalysts [94]. According to our results, when Rh loading is exceeding the concentration necessary to fulfill ~25–30% of a monolayer coverage, the noble metal is prone to volatilization and migration to other catalyst components, i.e. Al_2O_3 support in the downstream bed or in the washcoat. In contrast, Rh is stabilized in the Rh/Al_2O_3 catalyst and no migration was identified in the analogous experiment with the CeZrLa support located downstream of the Rh/Al_2O_3 catalyst. This behavior is supported also by the DFT calculations for adsorbed and substituted RhO_x species on the γ-Al_2O_3 (110) and θ-Al_2O_3 (100) surfaces. While the γ-Al_2O_3 (110) surface is relevant for the as prepared catalyst state, the θ-Al_2O_3 (100) surface is the most stable surface termination (surface free energy 0.042 eV/$Å^2$) that is present in the hydrothermally aged Rh/Al_2O_3 catalyst. Even at low to moderate temperatures, water adsorption on γ-Al_2O_3 seems to hinder the formation of Rh single sites (Fig. 2). According to our DFT calculation (Table S5), the dissociative adsorption of water was found to be with 0.75 eV more favorable than molecular adsorption on γ-Al_2O_3 (110). In contrast, molecular bonding of H_2O is more favorable (0.5 eV) than dissociative adsorption on θ-Al_2O_3(100). Hence, the higher surface free energy of γ-Al_2O_3 (110) (0.164 eV/Å2) likely enhances the process of dissociative H_2O adsorption and prevents Rh substitution in the γ-Al_2O_3 surface at moderate temperatures. After the phase transition of γ-Al_2O_3 at elevated temperatures, the resulting θ-Al_2O_3 (100) surface with very low surface

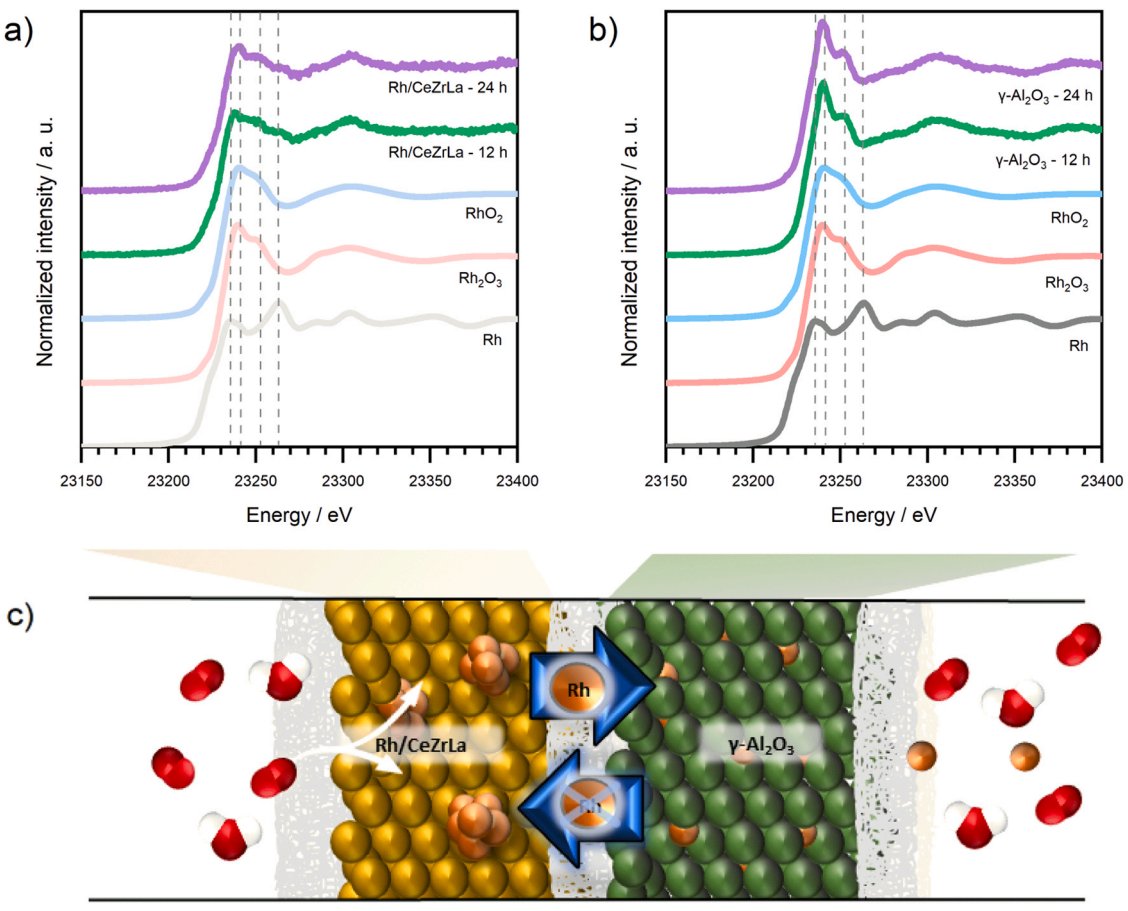

Fig. 10. XANES spectra collected at the Rh K-edge for the Rh/CeZrLa (a) and Rh/γ-Al_2O_3 (b) samples after aging for 12 or 24 h in hydrothermal atmosphere (10% O_2, 5% H_2O / N_2) at 1050 °C. XANES spectra of Rh references are depicted for comparison. The aging protocol, which is illustrated in (c), involved a plug-flow reactor with two catalyst beds, i.e. Rh/CeZrLa and Rh/γ-Al_2O_3, separated by quartz wool.

free energy does not seem to support water dissociation, potentially enabling single site formation by substitution. In this regard, further DFT calculations show that whereas γ-Al_2O_3 (110) facet is strongly hydroxylated across the entire temperature range the adsorption and substitution of individual RhO_2 species are unfavorable on this strongly hydroxylated surface (Figure S18a). On the θ-Al_2O_3(100) surface, dissociative adsorption of H_2O is not favorable on either the plain surface or the surface substituted with $RhO_{1.5}$ and does not stabilize the adsorbed RhO_2 species (Figure S18b).

Two types of Al species are present on the θ-Al_2O_3 (100) surface – octahedrally and tetrahedrally coordinated. As shown in Figure S17, a significantly stronger interaction is exhibited especially between the substituted noble metal species and alumina surface in comparison to the CeO_2 and ZrO_2 counterparts (Fig. S16 and S17). In this regard, the stability of substituted $RhO_{2.5}$ and $RhO_{1.5}$ on the γ-Al_2O_3 (110) surface is similar or even slightly higher in comparison to that of bulk RhO_2 (Fig. S15). At the same time, $RhO_{1.5}$ substituted species into octahedrally coordinated Al sites in the first subsurface layer are the most stable for the θ-Al_2O_3 (100) surface (Table S3). However, as shown by the differential substitution energy of $RhO_{1.5}$ species into octahedrally coordinated sites in the first subsurface layer (Table S4), any increase of the substitution extent leads to system destabilization. This trend suggests that Rh accommodation into the θ-Al_2O_3 lattice is concentration limited. Nevertheless, for the low noble metal loadings used in this study, the diffusion of Rh is probably completed at high temperatures, as indicated by the analysis of the XAS data obtained for the aged samples (Figs. 9 and S10).

Hence, the transfer and redistribution of Rh from the CeZrLa to the θ-Al_2O_3 support via the vapor phase (probably assisted by H_2O in the feed) is at least partially possible above 950 °C under oxidizing conditions (lean) besides the surface migration of metallic Rh particles between different catalyst components during the stoichiometric/rich steps of the fuel-cut procedure. This combined ageing mechanism could explain the homogeneous distribution of Rh on both supports and the presence of relatively small NM particles despite the harsh fuel-cut ageing conditions (Figs. 6 and S6). Furthermore, additional elemental analysis of hydrothermally aged BM: Rh/Al_2O_3-CeZrLa and BM: Rh/CeZrLa-Al_2O_3 washcoats at 1050 °C indicate that due to the close interaction between the washcoat components, the noble metal loss is prevented. According to the noble metal concentrations reported in Table 1 for the fresh and hydrothermally aged washcoats, almost identical Rh amounts are present in both samples. This outcome is in line with the structural peculiarities revealed for the *ex situ* and *in situ* aged washcoats and also by the regained catalytic activity during the following light-off test to 800 °C (Fig. 8).

4. Conclusions

Complementary *in situ/operando* characterization methods and extensive catalytic tests allowed to decipher the evolution of Rh state in γ-Al_2O_3/CeO_2-ZrO_2-La_2O_3 supported three-way catalyst washcoats under reaction conditions and thermal/chemical stress as a function of the initial noble metal location. Corresponding unmixed Rh/CeZrLa or Rh/γ-Al_2O_3 catalysts were also studied in order to differentiate the individual impact of each support. In addition to light-off/light-out cycles within different temperature windows, fuel-cut and hydrothermal ageing conditions were applied to investigate the noble metal structural dynamics in unmixed, mixed and spatially separated washcoat

components.

Highly dispersed Rh^{4+} species were found on the unmixed CeZrLa support in the as prepared catalyst whereas Rh_2O_3 nanoparticles are present on the γ-Al_2O_3 support after calcination at 500 °C in static air. Due to the contribution of the Rh-CeZrLa perimeter sites, a lower onset temperature was exhibited by the as prepared Rh/CeZrLa catalyst during CO oxidation in comparison to the Rh/γ-Al_2O_3 sample. The type of catalyst carrier does not seem to have a major impact on the NO and C_3H_6 conversion, which proceeded simultaneously with the noble metal reduction. After catalyst degreening during several light-off/light-out cycles and formation of metallic Rh nanoparticles, an improved activity was displayed by the alumina-supported sample. An analogous noble metal evolution and catalytic performance were identified for the corresponding washcoats.

During the fuel-cut ageing procedure at 1000 °C, which involved switches between the stoichiometric reaction mixture and O_2-rich atmosphere, a pronounced redox response was uncovered by *operando* XAS measurements for the Rh species supported on alumina whereas only 50% of Rh was redox active on the CeZrLa support. This behaviour was correlated with a limited interaction of Rh species with CeZrLa at high temperatures, which resulted in sintering of Rh nanoparticles under stoichiometric reaction conditions. On the contrary, the interplay between Rh and alumina is enhanced at high temperatures simultaneously with the phase transformation of γ-Al_2O_3 to θ-Al_2O_3, leading to the formation of $RhAlO_x$-like composites during exposure to O_2-rich conditions. According to DFT calculations, this intermixing corresponds to the formation of substituted $RhO_{1.5}$ species into the first subsurface layer of θ-Al_2O_3 (100) surface. Noteworthy was the similar behaviour of both Rh/Al_2O_3-CeZrLa and Rh/CeZrLa-Al_2O_3 washcoats with that exhibited by the alumina-supported catalyst, which could be correlated with partial relocation of Rh species already during the short fuel-cut procedure.

Regardless of the initial noble metal location in the parent catalyst, Rh migration occurs at high temperatures in both directions in a rich/stoichiometric reaction mixture due to the formation of mobile metallic species that do not interact anymore with Al_2O_3 or CeZrLa supports. During this step of the fuel-cut procedure, the noble metal is also prone to sintering. In contrast, in an O_2-rich atmosphere at temperatures above 950 °C a part of Rh migrates also via the vapour phase from the CeZrLa support to the θ-Al_2O_3 component of the washcoat, where it is stabilized as an inactive $RhAlO_x$ phase. This latter path was confirmed by additional hydrothermal ageing tests of spatially separated catalyst beds. Furthermore, significant noble metal loss was identified for the hydrothermally aged unmixed Rh/CeZrLa catalyst after long-term hydrothermal ageing at 1050 °C. The remaining amount of noble metal seems to be present both as highly dispersed species and partially reduced nanoparticles, the extent of each state most probably depending on the support composition and the concentration of surface vacancies. For both Rh/Al_2O_3-CeZrLa and Rh/CeZrLa-Al_2O_3, the intimate interaction between the catalyst components prevents the loss of noble metal via volatilisation. Furthermore, such a system ensures reversibility of the deactivation process. During subsequent light-off/light-out cycles or lambda variations, $RhAlO_x$ composites are converted back into active Rh nanoparticles whereas sintered Rh nanoparticles can be redispersed via the strong interaction with alumina and, to a certain extent, with ceria-zirconia supports.

Overall, our systematic study involving detailed *in situ/operando* characterization uncovers that already during the short fuel-cut treatment the behaviour of Rh in Al_2O_3/CeO_2-ZrO_2-La_2O_3–based washcoats is highly dynamic, with a major impact on the catalytic activity. Herein, multiple effects need to be considered including the gas atmosphere and temperature, the sintering of the support, varying noble metal-support interactions, solid-state reactions and noble metal volatility. In this regard, lambda variation is an important process parameter for TWC applications and should be considered in a future study. These manifold and interconnected parameters, emphasized in this study for Rh, are expected to affect the state and performance of other noble metal-based washcoats in an analogous manner.

Declaration of Competing Interest

The authors declare that they have no known competing financial interests or personal relationships that could have appeared to influence the work reported in this paper.

Acknowledgements

We acknowledge SOLEIL for provision of synchrotron radiation facilities and we would like to thank V. Briois, S. Belin, A. Beauvois and L. Barthe at the ROCK beamline and E. Fonda, A. Zitolo and L. Gautier at the SAMBA beamline for their highly valuable support and assistance during our beamtimes (proposal number: 20201723, 20210570 and 20240762). This work was supported by a public grant overseen by the French National Research Agency (ANR) as part of the "Investissements d'Avenir" program (reference: ANR-10-EQPX-45). We acknowledge the European Synchrotron Radiation Facility (ESRF) for provision of synchrotron radiation facilities and we would like to thank Dr. Kirill Lomachenko and Dr. Davide Salusso for their great support in using the BM23 – XAS Beamline.T. Bergfeldt (IAM-AWP, KIT) and Heike Störmer (LEM, KIT) for XRF analysis and electron microscopy measurements, respectively. The authors thank the State of Baden-Württemberg for its support through bwHPC and the German Research Foundation (DFG) for funding within the framework of project INST40/575-1FUGG (Cluster JUSTUS2, Research Resources bw17D011). JDG, FS, and MC thank the CRC1441 "TrackAct" for support (Project-ID 426888090). AK Grunwaldt colleagues are acknowledged for their great support during synchrotron measurements.

Appendix A. Supporting information

Supplementary data associated with this article can be found in the online version at doi:10.1016/j.apcatb.2026.126851.

Data availability

Data will be made available on request.

References

[1] J.A. Farmer, C.T. Campbell, Ceria maintains smaller metal catalyst particles by strong metal-support bonding, Science 329 (2010) 933–936, https://doi.org/10.1126/science.1191778.
[2] E. Ruckenstein, D.B. Dadyburjor, Sintering and redispersion in supported metal catalysts, Rev. Chem. Eng. 1 (1983) 251–356, https://doi.org/10.1016/S0167-2991(08)65162-9.
[3] H. Shinjoh, et al., Suppression of noble metal sintering based on the support anchoring effect and its application in automotive three-way catalysis, Top. Catal. 52 (2009) 1967–1971, https://doi.org/10.1007/s11244-009-9371-5.
[4] Y. Nagai, et al., situ redispersion of platinum autoexhaust catalysts: an on-line approach to increasing catalyst lifetimes, Angew. Chem. Int. Ed. 47 (2008) 9303–9306, https://doi.org/10.1002/anie.200803126.
[5] A.M. Gänzler, et al., Tuning the structure of platinum particles on ceria in situ for enhancing the catalytic performance of exhaust gas catalysts, Angew. Chem. Int. Ed. 56 (2017) 13078–13082, https://doi.org/10.1002/anie.201707842.
[6] D. Gashnikova, et al., Highly active oxidation catalysts through confining Pd clusters on CeO_2 Nano-Islands, Angew. Chem. Int. Ed. 63 (2024) e202408511, https://doi.org/10.1002/anie.202408511.
[7] F. Maurer, et al., Tracking the formation, fate and consequence for catalytic activity of Pt single sites on CeO_2, Nat. Catal. 3 (2020) 824–833, https://doi.org/10.1038/s41929-020-00508-7.
[8] E.A. Fedorova, et al., Unraveling the low-temperature activity of Rh–CeO_2 catalysts in CO oxidation: probing the local structure and Red-Ox transformation of Rh^{3+} species. *PCCP* 25 (2023) 2862–2874, https://doi.org/10.1039/D2CP04503F.
[9] R. Alcala, et al., Atomically dispersed dopants for stabilizing ceria surface area, Appl. Catal. B 284 (2021) 119722, https://doi.org/10.1016/j.apcatb.2020.119722.
[10] B. Li, et al., Origin of Rh and Pd agglomeration on the CeO_2 (111) surface, Phys. Rev. B 82 (2010) 125422, https://doi.org/10.1103/PhysRevB.82.125422.

[11] H. Mizoguchi, L.N. Zakharov, N.S.P. Bhuvanesh, A.W. Sleight, M.A. Subramanian, Synthesis and crystal structure of two new cerium rhodium oxides: $Ce_{2/3-x}Rh_2^{3+}O_4$ (x~0.12) with Ce mixed valency and $Ce^{4+}Rh_2^{3+}O_5$, J. Solid State Chem. 184 (2011) 1381–1386, https://doi.org/10.1016/j.jssc.2011.04.005.

[12] L.S. Kibis, et al., Redox and catalytic properties of $Rh_xCe_{1-x}O_{2-\delta}$ solid solution, J. Phys. Chem. C. 121 (2017) 26925–26938, https://doi.org/10.1021/acs.jpcc.7b09983.

[13] K. Jacob, S. Muraleedharan, Phase diagram of the system Ce-Rh-O, Calphad 65 (2019) 171–176, https://doi.org/10.1016/j.calphad.2019.02.013.

[14] M. Machida, et al., Thermal Aging of Rh/ZrO_2–CeO_2 three-way catalysts under dynamic lean/rich perturbation accelerates deactivation via an encapsulation mechanism, ACS Catal. 13 (2023) 3806–3814, https://doi.org/10.1021/acscatal.2c06289.

[15] H.C. Yao, S. Japar, M. Shelef, Surface interactions in the system $RhAl_2O_3$, J. Catal. 50 (1977) 407–418, https://doi.org/10.1016/0021-9517(77)90053-7.

[16] C. Wong, & McCabe, R. W. Effects of high-temperature oxidation and reduction on the structure and activity of $RhAl_2O_3$ and $RhSiO_2$ catalysts, J. Catal. 119 (1989) 47–64, https://doi.org/10.1016/0021-9517(89)90133-4.

[17] R. Burch, P.K. Loader, N.A. Cruise, An investigation of the deactivation of Rh/alumina catalysts under strong oxidising conditions, Appl. Catal. A 147 (1996) 375–394, https://doi.org/10.1016/S0926-860X(96)00212-8.

[18] C.-P. Hwang, C.-T. Yeh, Q. Zhu, Rhodium-oxide species formed on progressive oxidation of rhodium clusters dispersed on alumina, Catal. Today 51 (1999) 93–101, https://doi.org/10.1016/S0920-5861(99)00011-5.

[19] D. Beck, T. Capehart, C. Wong, D. Belton, XAFS characterization of Rh/Al_2O_3 after treatment in high-temperature oxidizing environments, J. Catal. 144 (1993) 311–324, https://doi.org/10.1006/jcat.1993.133.

[20] Z. Weng-Sieh, R. Gronsky, A.T. Bell, Effects of support interaction on the phase stability of Rh oxides formed during the aging of α-alumina supported Rh in air, J. Catal. 174 (1998) 22–33, https://doi.org/10.1006/jcat.1997.1944.

[21] C.-H. Li, J. Wu, A.B. Getsoian, G. Cavataio, J.R. Jinschek, Direct observation of rhodium aluminate (RhAlOx) and its role in deactivation and regeneration of Rh/Al_2O_3 under three-way catalyst conditions, Chem. Mater. 34 (2022) 2123–2132, https://doi.org/10.1021/acs.chemmater.1c03513.

[22] T. Horiuchi, et al., Improvement of thermal stability of alumina by addition of zirconia, Catal. Lett. 62 (1999) 107–111, https://doi.org/10.1023/A:1019051123075.

[23] F. Oudet, P. Courtine, A. Vejux, Thermal stabilization of transition alumina by structural coherence with $LnAlO_3$ (Ln = La, Pr, Nd), J. Catal. 114 (1988) 112–120, https://doi.org/10.1016/0021-9517(88)90013-9.

[24] H. Schaper, E.B.M. Doesburg, L.L. Van Reijen, The influence of lanthanum oxide on the thermal stability of gamma alumina catalyst supports, Appl. Catal. 7 (1983) 211–220, https://doi.org/10.1016/0166-9834(83)80009-8.

[25] A. Trovarelli, Structural and oxygen storage/release properties of CeO_2-based solid solutions, Comments Inorg. Chem. 20 (1999) 263–284, https://doi.org/10.1080/02603599908021446.

[26] C. Andriopoulou, et al., Structural and redox properties of $Ce_{1-x}Zr_xO_{2-\delta}$ and $Ce_{0.8}Zr_{0.15}RE_{0.05}O_{2-\delta}$ (RE: La, Nd, Pr, Y) solids studied by high temperature in situ Raman spectroscopy, J. Phys. Chem. C. 121 (2017) 7931–7943, https://doi.org/10.1021/acs.jpcc.7b00515.

[27] Y. Zhou, et al., Synthesis and study of nanostructured Ce-Zr-La-RE-O (RE= Y, Nd and Pr) quaternary solid solutions and their supported three-way catalysts, Mater. Des. 130 (2017) 149–156, https://doi.org/10.1016/j.matdes.2017.05.059.

[28] S. Li, et al., Synthesis of a homogeneous CeO_2–ZrO_2-Al_2O_3 composite material by a novel hydrothermal assisted precipitation method, Mol. Catal. 551 (2023) 113660, https://doi.org/10.1016/j.mcat.2023.113660.

[29] A. Morikawa, et al., A new concept in high performance ceria–zirconia oxygen storage capacity material with Al_2O_3 as a diffusion barrier, Appl. Catal. B 78 (2008) 210–221, https://doi.org/10.1016/j.apcatb.2007.09.013.

[30] M. Votsmeier, T. Kreuzer, J. Gieshoff, G. Lepperhoff, Automobile exhaust control, Ullmann's. Encycl. Ind. Chem. 4 (2009) 407–424, https://doi.org/10.1002/14356007.a03_189.pub2.

[31] M. Ozawa, T. Okouchi, M. Haneda, Three way catalytic activity of thermally degenerated Pt/Al_2O_3 and Pt/CeO_2–ZrO_2 modified Al_2O_3 model catalysts, Catal. Today 242 (2015) 329–337, https://doi.org/10.1016/j.cattod.2014.06.013.

[32] W. Tan, et al., Highly efficient Pt catalyst on newly designed CeO_2-ZrO_2-Al_2O_3 support for catalytic removal of pollutants from vehicle exhaust, Chem. Eng. J. 426 (2021) 131855, https://doi.org/10.1016/j.cej.2021.131855.

[33] I. Morita, et al., Effective utilization of Pt catalyst in three-way catalytic system by employing calcined ceria with alumina, SAE Tech. Pap. (2024), https://doi.org/10.4271/2024-01-2133, 0148-7191.

[34] S. Colussi, et al., Structure and morphology of Pd/Al_2O_3 and Pd/CeO_2/Al_2O_3 combustion catalysts in Pd–PdO transformation hysteresis, Appl. Catal. A 390 (2010) 1–10, https://doi.org/10.1016/j.apcata.2010.09.033.

[35] K. Chen, J. Wan, J. Lin, R. Zhou, Comparative study of three-way catalytic performance over Pd/CeO_2-ZrO_2-Al_2O_3 and Pd/La-Al_2O_3 catalysts: new insights into microstructure and thermal stability, Mol. Catal. 526 (2022) 112361, https://doi.org/10.1016/j.mcat.2022.112361.

[36] R. Jiang, et al., Recent progress of Rh-based three-way catalysts, Smart Mol. 2 (2024) e20240004, https://doi.org/10.1002/smo.20240004.

[37] Y. Tomida, M. Haneda, A study of ageing effect: migration of rhodium under air atmosphere, Catal. Today 376 (2021) 81–86, https://doi.org/10.1016/j.cattod.2020.07.083.

[38] B. Ravel, M. Newville, ATHENA, ARTEMIS, HEPHAESTUS: data analysis for X-ray absorption spectroscopy using IFEFFIT, J. Synchrotron Radiat. 12 (2005) 537–541.

[39] G. Landrot, FASTOSH: a software to process XAFS data for geochemical & environmental applications, Goldschmidt Abstr. 1402 (2018), https://doi.org/10.1107/S1600577525003923.

[40] H. Funke, A.C. Scheinost, M. Chukalina, Wavelet analysis of extended x-ray absorption fine structure data, Phys. Rev. B 71 (2005) 094110, https://doi.org/10.1103/PhysRevB.71.094110.

[41] Z. Xia, H. Zhang, K. Shen, Y. Qu, Z. Jiang, Wavelet analysis of extended X-ray absorption fine structure data: theory, application, Phys. B 542 (2018) 12–19, https://doi.org/10.1016/j.physb.2018.04.039.

[42] G. Kresse, J. Furthmüller, Efficiency of ab-initio total energy calculations for metals and semiconductors using a plane-wave basis set, Comput. Mater. Sci. 6 (1996) 15–50, https://doi.org/10.1016/0927-0256(96)00008-0.

[43] G. Kresse, J. Furthmüller, Efficient iterative schemes for ab initio total-energy calculations using a plane-wave basis set, Phys. Rev. B 54 (1996) 11169, https://doi.org/10.1103/PhysRevB.54.11169.

[44] A.H. Larsen, et al., The atomic simulation environment—a Python library for working with atoms, J. Phys. Condens. Matter 29 (2017) 273002, https://doi.org/10.1088/1361-648X/aa680e.

[45] P.E. Blöchl, Projector augmented-wave method, Phys. Rev. B 50 (1994) 17953–17979, https://doi.org/10.1103/PhysRevB.50.17953.

[46] G. Kresse, D. Joubert, From ultrasoft pseudopotentials to the projector augmented-wave method, Phys. Rev. B 59 (1999) 1758–1775, https://doi.org/10.1103/PhysRevB.59.1758.

[47] J.J. Mortensen, et al., Bayesian error estimation in density-functional theory, Phys. Rev. Lett. 95 (2005) 216401, https://doi.org/10.1103/PhysRevLett.95.216401.

[48] H.J. Monkhorst, J.D. Pack, Special points for Brillouin-zone integrations, Phys. Rev. B 13 (1976) 5188–5192, https://doi.org/10.1103/PhysRevB.13.5188.

[49] M. Digne, P. Sautet, P. Raybaud, P. Euzen, H. Toulhoat, Use of DFT to achieve a rational understanding of acid–basic properties of γ-alumina surfaces, J. Catal. 226 (2004) 54–68, https://doi.org/10.1016/j.jcat.2004.04.020.

[50] C.E. García-Vargas, et al., Highly active and stable single atom Rh_1/CeO_2 catalyst for CO oxidation during redox cycling, ChemCatChem 15 (2023) e202201210, https://doi.org/10.1002/cctc.202201210.

[51] B.B. Sarma, et al., One-pot cooperation of single-atom Rh and Ru solid catalysts for a selective Tandem Olefin isomerization-hydrosilylation process, Angew. Chem. Int. Ed. 59 (2020) 5806–5815, https://doi.org/10.1002/anie.201915255.

[52] J. Wu, A.E. O'Neill, C.-H. Li, J.R. Jinschek, G. Cavataio, Superior TWC activity of Rh supported on pyrochlore-phase ceria zirconia, Appl. Catal. B 280 (2021) 119450, https://doi.org/10.1016/j.apcatb.2020.119450.

[53] L.S. Kibis, et al., From highly dispersed Rh^{3+} to nanoclusters and nanoparticles: Probing the low-temperature NO+ CO activity of Rh-doped CeO_2 catalysts, Appl. Surf. Sci. 493 (2019) 1055–1066, https://doi.org/10.1016/j.apsusc.2019.07.043.

[54] A.M. Gänzler, et al., Unravelling the different reaction pathways for low temperature CO oxidation on Pt/CeO_2 and Pt/Al_2O_3 by spatially resolved structure–activity correlations, J. Phys. Chem. Lett. 10 (2019) 7698–7705, https://doi.org/10.1021/acs.jpclett.9b02768.

[55] Y.-F.Y. Yao, The oxidation of CO and hydrocarbons over noble metal catalysts, J. Catal. 87 (1984) 152–162, https://doi.org/10.1016/0021-9517(84)90178-7.

[56] R. Kopelent, et al., Catalytically active and spectator Ce^{3+} in ceria-supported metal catalysts, Angew. Chem. 127 (2015) 8852–8855, https://doi.org/10.1002/anie.201503022.

[57] M. Cargnello, et al., Control of metal nanocrystal size reveals metal-support interface role for ceria catalysts, Science 341 (2013) 771–773, https://doi.org/10.1126/science.1240148.

[58] N. Bosio, M. Di, M. Skoglundh, P.-A. Carlsson, H. Gronbeck, Interface reactions dominate low-temperature CO oxidation activity over Pt/CeO_2, J. Phys. Chem. C. 126 (2022) 16164–16171, https://doi.org/10.1021/acs.jpcc.2c04833.

[59] L. Artiglia, et al., Introducing time resolution to detect Ce^{3+} catalytically active sites at the Pt/CeO_2 interface through ambient pressure X-ray photoelectron spectroscopy, J. Phys. Chem. Lett. 8 (2017) 102–108, https://doi.org/10.1021/acs.jpclett.6b02314.

[60] K.T. Jacob, S. Muraleedharan, Phase diagram of the system Ce-Rh-O, Calphad 65 (2019) 171–176, https://doi.org/10.1016/j.calphad.2019.02.013.

[61] A. Fathali, F. Wallin, A. Kristoffersson, M. Laurell, Thermal and chemical deactivation of three-way catalysts: comparison of road-, fuel-cut and SAI-aged catalysts, SAE Tech. Pap. (2015), https://doi.org/10.4271/2015-01-1000.

[62] A. Fathali, M. Laurell, B. Andersson, Fuel-cut based rapid aging of commercial three way catalysts-Influence of fuel-cut frequency, duration and temperature on catalyst activity, SAE Tech. Pap. (2013), https://doi.org/10.4271/2013-24-0156.

[63] A.K. Datye, Q. Xu, K.C. Kharas, J.M. McCarty, Particle size distributions in heterogeneous catalysts: What do they tell us about the sintering mechanism? Catal. Today 111 (2006) 59–67, https://doi.org/10.1016/j.cattod.2005.10.013.

[64] M. Machida, et al., Rh nanoparticles dispersed on ZrO_2–CeO_2 migrate to Al_2O_3 supports to mitigate thermal deactivation via encapsulation, ACS Appl. Nano Mater. (2023), https://doi.org/10.1021/acsanm.3c01535.

[65] L. Carol, G. Mann, High-temperature oxidation of rhodium, Oxid. Met. 34 (1990) 1–12.

[66] H. Nose, et al., Fuel enrichment control system by catalyst temperature estimation to enable frequent stoichiometric operation at high engine speed/load condition, 0148-7191, SAE Tech. Paper, 2013, https://doi.org/10.4271/2013-01-0341.

[67] A.V. Porsin, et al., A destruction mechanism of a three-way catalyst due to a failure of fuel supply in a spark ignition engine, Emiss. Control Sci. Technol. 7 (2021) 163–173, https://doi.org/10.1007/s40825-021-00187-1.

[68] R. Möller, M. Votsmeier, C. Onder, L. Guzzella, J. Gieshoff, Is oxygen storage in three-way catalysts an equilibrium controlled process? Appl. Catal. B 91 (2009) 30–38, https://doi.org/10.1016/j.apcatb.2009.05.003.

[69] Trovarelli, A. *Catalysis by ceria and related materials*. Vol. 2 (World Scientific, 2002), doi: https://doi.org/10.1142/p249.
[70] D. Duprez, C. Descorme, T. Birchem, E. Rohart, Oxygen storage and mobility on model three-way catalysts, Top. Catal. 16 (2001) 49–56, https://doi.org/10.1023/A:1016622612521.
[71] A.M. Gänzler, et al., Tuning the Pt/CeO_2 interface by in situ variation of the Pt particle size, ACS Catal. 8 (2018) 4800–4811, https://doi.org/10.1021/acscatal.8b00330.
[72] G. Jiaxiu, et al., Study of Pt–Rh/CeO_2–ZrO_2–M_xO_y (M=Y, La)/Al_2O_3 three-way catalysts, Appl. Surf. Sci. 273 (2013) 527–535, https://doi.org/10.1016/j.apsusc.2013.02.074.
[73] P. Fornasiero, et al., Rh-Loaded CeO_2-ZrO_2 solid-solutions as highly efficient oxygen exchangers: dependence of the reduction behavior and the oxygen storage capacity on the structural-properties, J. Catal. 151 (1995) 168–177, https://doi.org/10.1006/jcat.1995.1019.
[74] M. Fernández-García, et al., Structural characteristics and redox behavior of CeO_2–ZrO_2/Al_2O_3 supports, J. Catal. 194 (2000) 385–392, https://doi.org/10.1006/jcat.2000.2931.
[75] A. Morikawa, K. Kikuta, A. Suda, H. Shinjo, Enhancement of oxygen storage capacity by reductive treatment of Al_2O_3 and CeO_2–ZrO_2 solid solution nanocomposite, Appl. Catal. B 88 (2009) 542–549, https://doi.org/10.1016/j.apcatb.2008.10.019.
[76] H. Vidal, et al., Redox behavior of CeO_2-ZrO_2 mixed oxides. I. Influence of redox treatments on high surface area catalysts, Appl. Catal. B 27 (2000) 49–63.
[77] J. Kašpar, S. Bernal, A. Cordón, V. Perrichon, F. Fally, Redox behavior of CeO_2–ZrO_2 mixed oxides: I. Influence of redox treatments on high surface area catalysts, Appl. Catal. B 27 (2000) 49–63, https://doi.org/10.1016/S0926-3373(00)00138-7.
[78] P. Fornasiero, G.R. Rao, J. Kašpar, F. L'Erario, M. Graziani, Reduction of NO by CO over Rh/CeO_2–ZrO_2 catalysts: evidence for a support-promoted catalytic activity, J. Catal. 175 (1998) 269–279, https://doi.org/10.1006/jcat.1998.1999.
[79] V. Perrichon, A. Laachir, S. Abouarnadasse, O. Touret, G. Blanchard, Thermal stability of a high surface area ceria under reducing atmosphere, Appl. Catal. A 129 (1995) 69–82, https://doi.org/10.1016/0926-860X(95)00089-5.
[80] V. Marchionni, et al., A modulated excitation ED-EXAFS/DRIFTS study of hydrothermal ageing of Rh/Al_2O_3, Catal. Today 229 (2014) 80–87, https://doi.org/10.1016/j.cattod.2013.10.082.
[81] M. Munoz, P. Argoul, F. Farges, Continuous Cauchy wavelet transform analyses of EXAFS spectra: a qualitative approach, Am. Miner. 88 (2003) 694–700, https://doi.org/10.2138/am-2003-0423.
[82] J. Timoshenko, A. Kuzmin, Wavelet data analysis of EXAFS spectra, Comput. Phys. Commun. 180 (2009) 920–925, https://doi.org/10.1016/j.cpc.2008.12.020.
[83] J.G. Chen, M.L. Colaianni, P. Chen, J.T. Yates, G.B. Fisher, Thermal behavior of a rhodium/alumina model catalyst: disappearance of surface rhodium upon heating, J. Phys. Chem. 94 (1990) 5059–5062, https://doi.org/10.1021/j100375a055.
[84] A. Powell, Behaviour of the platinum metals at high temperatures, Platin. Met. Rev. 2 (1958) 95–98, https://doi.org/10.1595/003214058X239598.
[85] H. Jehn, High temperature behaviour of platinum group metals in oxidizing atmospheres, J. Less Common Met. 100 (1984) 321–339, https://doi.org/10.1016/0022-5088(84)90072-9.
[86] M. Rubel, M. Pszonicka, M.F. Ebel, A. Jabłoński, W. Palczewska, Oxygen generated platinum, rhodium and palladium volatile losses from pure metals and their alloys, J. Less Common Met. 125 (1986) 7–24, https://doi.org/10.1016/0022-5088(86)90076-7.
[87] G. Ferré, et al., Exploiting the dynamic properties of Pt on ceria for low-temperature CO oxidation, Catal. Sci. Technol. 10 (2020) 3904–3917, https://doi.org/10.1039/D0CY00732C.
[88] D. Zengel, et al., Pd loading threshold for an efficient noble metal use in Pd/CeO_2 methane oxidation catalysts, Appl. Catal. B 358 (2024) 124363, https://doi.org/10.1016/j.apcatb.2024.124363.
[89] F. Maurer, et al., Surface noble metal concentration on ceria as a key descriptor for efficient catalytic CO oxidation, ACS Catal. 12 (2022) 2473–2486, https://doi.org/10.1021/acscatal.1c04565.
[90] H.V. Thang, G. Pacchioni, On the real nature of rh single-atom catalysts dispersed on the ZrO_2 surface, ChemCatChem 12 (2020) 2595–2604, https://doi.org/10.1002/cctc.201901878.
[91] Y. Cao, et al., Ageing resistance of rhodium supported on CeO_2–ZrO_2 and ZrO_2: Rhodium nanoparticle structure and Rh–support interaction under diverse ageing atmosphere, Catal. Today 281 (2017) 490–499, https://doi.org/10.1016/j.cattod.2016.07.001.
[92] K.T. Jacob, Y. Waseda, Phase relations in the system La-Rh-O and thermodynamic properties of LaRhO3, J. Am. Ceram. Soc. 78 (1995) 440–444, https://doi.org/10.1111/j.1151-2916.1995.tb08821.x.
[93] T. Tanabe, et al., The interaction between supported Rh- and Nd_2O_3-enriched surface layer on ZrO2 for Rh sintering suppression, Catal. Today 184 (2012) 219–226, https://doi.org/10.1016/j.cattod.2011.10.005.
[94] J. Lee, et al., Influence of the defect concentration of ceria on the Pt dispersion and the CO oxidation activity of Pt/CeO_2, J. Phys. Chem. C. 122 (2018) 4972–4983, https://doi.org/10.1021/acs.jpcc.8b00254.